AD-A262 127

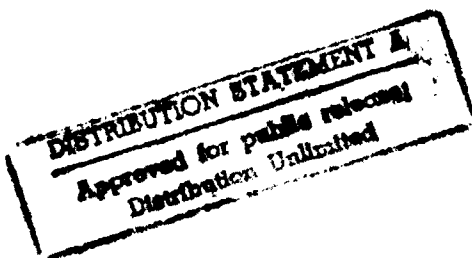# A Statistical Characterization of Denver-Area Microbursts

Kimberly L. Elmore
John McCarthy

National Center for Atmospheric Research
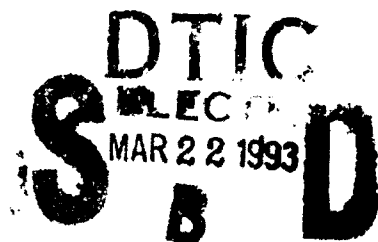P. O. Box 3000
Boulder, Colorado 80307

March 1989
Printed December 1992

Final Report

DTIC
ELECT
MAR 2 2 1993
S
B
D

U.S. Department
of Transportation

Federal Aviation
Administration

93-05837

93 3 19 012

NOTICE

This document is disseminated under the sponsorship of the Department of Transportation in the interest of information exchange. The U.S. Government assumes no liability for its contents or use thereof.

1. Report No. DOT/FAA/NR-92/13	2. Government Accession No.	3. Recipient's Catalog No.
4. Title and Subtitle A Statistical Characterization of Denver-Area Microbursts		5. Report Date March 1989/Print Dec 1992
		6. Performing Organization Code
7. Author's) Kimberly L. Elmore and John McCarthy		8. Performing Organization Report No.
9. Performing Organization Name and Address Joint Airport Weather Studies (JAWS) Project Research Applications Program National Center for Atmospheric Research P.O. Box 3000 Boulder, Colorado 80307		10. Work Unit No. (TRAIS)
		11. Contract or Grant No. DTFA01-82-Y-10513
12. Sponsoring Agency Name and Address U.S. Department of Trasportation Federal Aviation Administration		13. Type of Report and Period Covered Final Report
		14. Sponsoring Agency Code ANR-150

15. Supplementary Notes

Research performed under Interagency Agreement No. DTFA01-82-Y-10513 between the National Science Foundation and the Department of Transportation, Federal Aviation Administration

16. Abstract

This document describes statistical characteristics of microbursts that occurred in the Denver area during the summers of 1982 and 1984. The Joint Airport Weather Studies (JAWS) Project, conducted between 15 May and 13 August 1982, is the primary data source for this report, and radar data from the Classify, Locate and Avoid Wind Shear (CLAWS) Project are also included for microburst lines and low-reflectivity microbursts. All surface mesonet data come from the JAWS Project. This report describes the statistical characteristics of the JAWS and CLAWS data that have been analyzed to date and is intended to be used as a working document. It is primarily a compendium of several different sources brought together in a single document.

17. Key Words microburst, microburst line, JAWS, CLAWS, Denver area, statistical characteristics, ground-based sensors, parent storm structure, radar-derived statistics		18. Distribution Statement This document is available to the public through the National Technical Information Service, Springfield, Virginia 22161.	
19. Security Classif. (of this report) unclassified	20. Security Classif. (of this page) unclassified	21. No. of Pages 54	22. Price

Form DOT F 1700.7 (8-72)   Reproduction of completed page authorized

TABLE OF CONTENTS

i

LIST OF FIGURES

LIST OF TABLES

1. Introduction

This document describes statistical characteristics of microbursts that occurred in the Denver area during the summers of 1982 and 1984. The Joint Airport Weather Studies (JAWS) Project, conducted between 15 May and 13 August 1982, is the primary data source for this report, and radar data from the Classify, Locate and Avoid Wind Shear (CLAWS) Project are also included for microburst lines and low-reflectivity microbursts. All surface mesonet data come from the JAWS Project.

Intended as a working document, this report describes the statistical characteristics of the JAWS and, to a lesser extent, CLAWS data that have been analyzed to date. It is primarily a compendium of several different sources brought together in a single document. This document represents a single source for almost all statistical meteorological characteristics, gleaned from the JAWS data set in particular.

This data base is not exhaustive, as many more microbursts occurred during these two projects than are discussed here. Criteria used for radar case selection often did not depend upon meteorology, and good scan coordination between radars may have been the determining factor in choosing a case for analysis. In other instances, there may have been simultaneous active events, but only one event could be scanned at a time. Such limitations and restrictions are considered in more detail in those sections relying upon radar data.

This report is principally composed of figures accompanied by short discussions. The figures are arranged into six general sections: Ground-Based Sensor Statistics; Radar-Derived General Statistics; Radar-Derived Statistics Associated with Velocity Maxima; Radar-Derived, Small-Sample Characteristics; Parent Storm Structure; and Microburst Lines.

2. Ground-Based Sensor Statistics

Data in this section come exclusively from the Portable Automated Mesonet (PAM) stations deployed during the JAWS Project. Each station records 1-min averages of temperature, pressure, dewpoint or relative humidity, wind speed and direction, and rainfall. The maximum wind gust and its direction within each minute is also recorded. Data were recorded on a 24-hr basis, unlike radar data, so these statistics closely represent the population of microbursts that occurred during JAWS in 1982. Bear in mind that typical PAM station spacing was 4 km, so it is probable that some small microburst events were not observed.

All figures and tables in this section are adapted from Bedard and LeFebvre (1986).

TABLE 2.1. Impacting microburst statistics derived from PAM data for 33 cases.

Parameter	Average (for all affected sites)	Range (over all affected sites)
Wind speed change	13.5 m s^{-1}	2.5 to 27.5 m s^{-1}
Wind vector change	20.7 m s^{-1}	10 to 37.5 m s^{-1}
Temperature change	−1.5°C	−9 to +5°C
Pressure change	0.66 mb	−1.50 to 2.00 mb
Dewpoint change	0°C	−7 to +7°C
Rain rate	0.28 mm min^{-1}	0 to 2.75 mm min^{-1}

This table shows statistics derived from 33 impacting microbursts, i.e., microbursts whose centers actually passed over a PAM station. The average wind speed change is 13.5 m s^{-1}, regardless of any direction change, and the range of changes is 2.5 to 27.5 m s^{-1}. The average wind vector change is 20.7 m s^{-1}, with a range of 10 to 37.5 m s^{-1}. The average temperature change as a microburst traverses a station is -1.5 °C, with a range of -9 to +5°C. Thus, not all microbursts are accompanied by temperature falls. The average pressure change is +0.66 mb, displaying a range of -1.5 to +2.0 mb. Thus, not all microbursts are accompanied by pressure rises. The average dewpoint temperature change is 0°C, with a range of -7°C to +7°C. Finally, the average rain rate associated with a microburst is 0.28 mm min^{-1}, with a range of 0 to 2.75 mm min^{-1}.

These statistics demonstrate that, although on the average microbursts have thermodynamic and hydrostatic characteristics similar to gravity current phenomena, such characteristics are not always observed.

TABLE 2.2. Near microburst statistics derived from PAM data for 119 cases.

Parameter	Average (for all affected sites)	Range (over all affected sites)
Wind speed change	9.2 m s^{-1}	0 to 22 m s^{-1}
Wind vector change	14.7 m s^{-1}	5 to 32.5 m s^{-1}
Temperature change	$-1.1°C$	-9 to $+4°C$
Pressure change	0.24 mb	-1.50 to 2.00 mb
Rain rate	0.26 mm min^{-1}	0 to 2.75 mm min^{-1}

Similar to Table 2.1, these statistics are for microbursts contained within the PAM network that did not pass directly over a station, defined as "near" cases. In this data set, each event affects at least two other stations, so more stations are actually involved in each statistic; 119 events qualified in this category. The average wind speed change associated with such a microburst is less than that for impacting cases, as expected: 9.2 m s^{-1}, with a range of 0 to 22.0 m s^{-1}. Similarly, the average wind vector change is 14.7 m s^{-1}, ranging from 5 to 32.5 m s^{-1}. The average temperature change is $-1.1°C$, somewhat less than for impacting cases, with a range of -9 to $+4°C$. The average pressure change is only one-third of the impacting cases: 0.24 mb with a range of -1.5 to +2.0 mb. The average rain rate is almost identical to the average rain rate for impacting microbursts, 0.26 mm min^{-1} with a range of 0 to 2.75 mm min^{-1}.

DISTRIBUTION OF MAXIMUM SPEED CHANGE
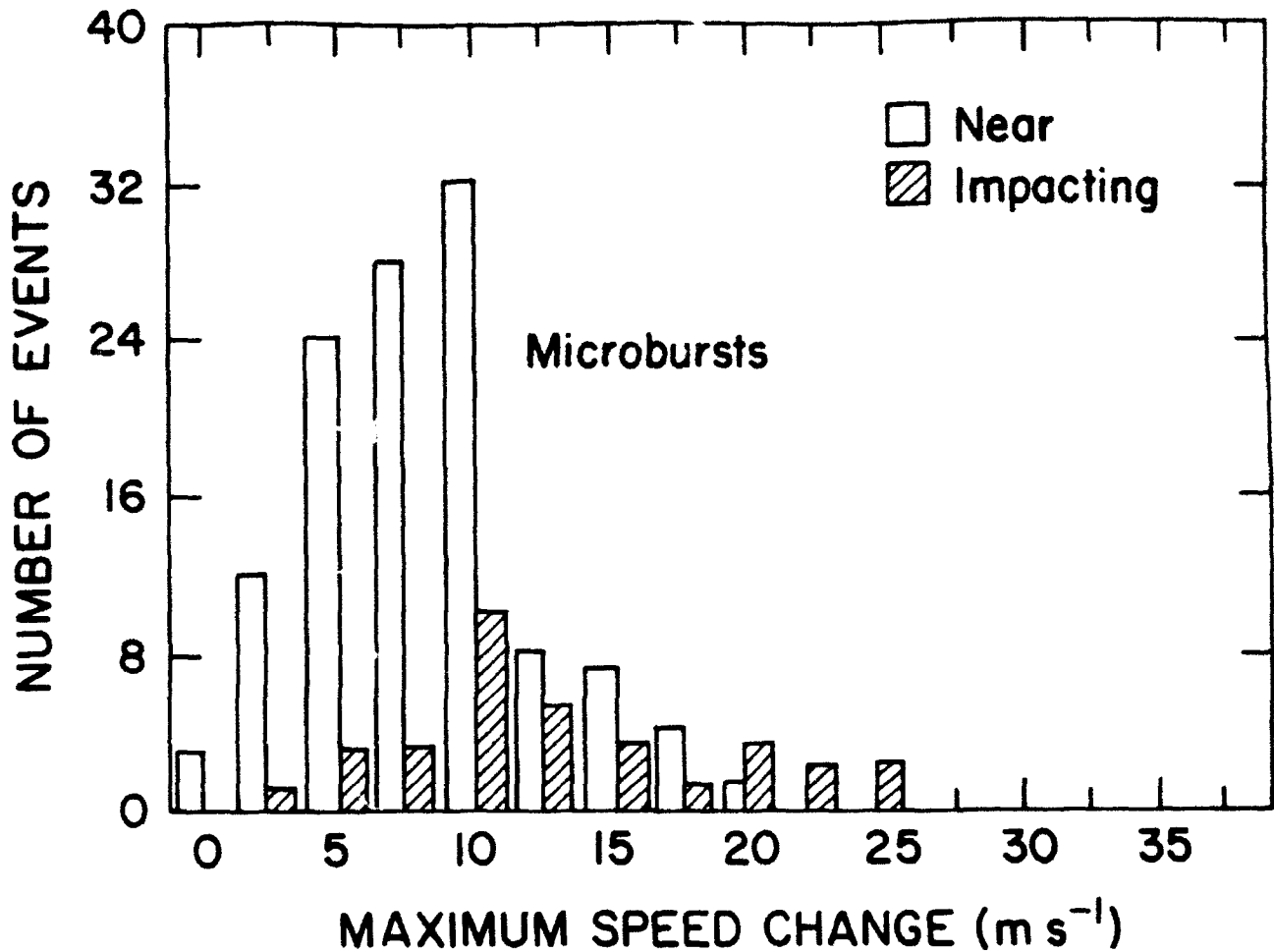
FIGURE 2.1. A frequency distribution showing the maximum wind speed change for impacting and near microbursts is shown in Fig. 2.1. For both types, the average maximum speed change is approximately 10 m s^{-1}. The impacting microbursts show the largest speed changes. For the near microbursts, the largest value of all affected sites for each event is used in plotting the frequency distribution.

DISTRIBUTION OF MAXIMUM VECTOR CHANGE
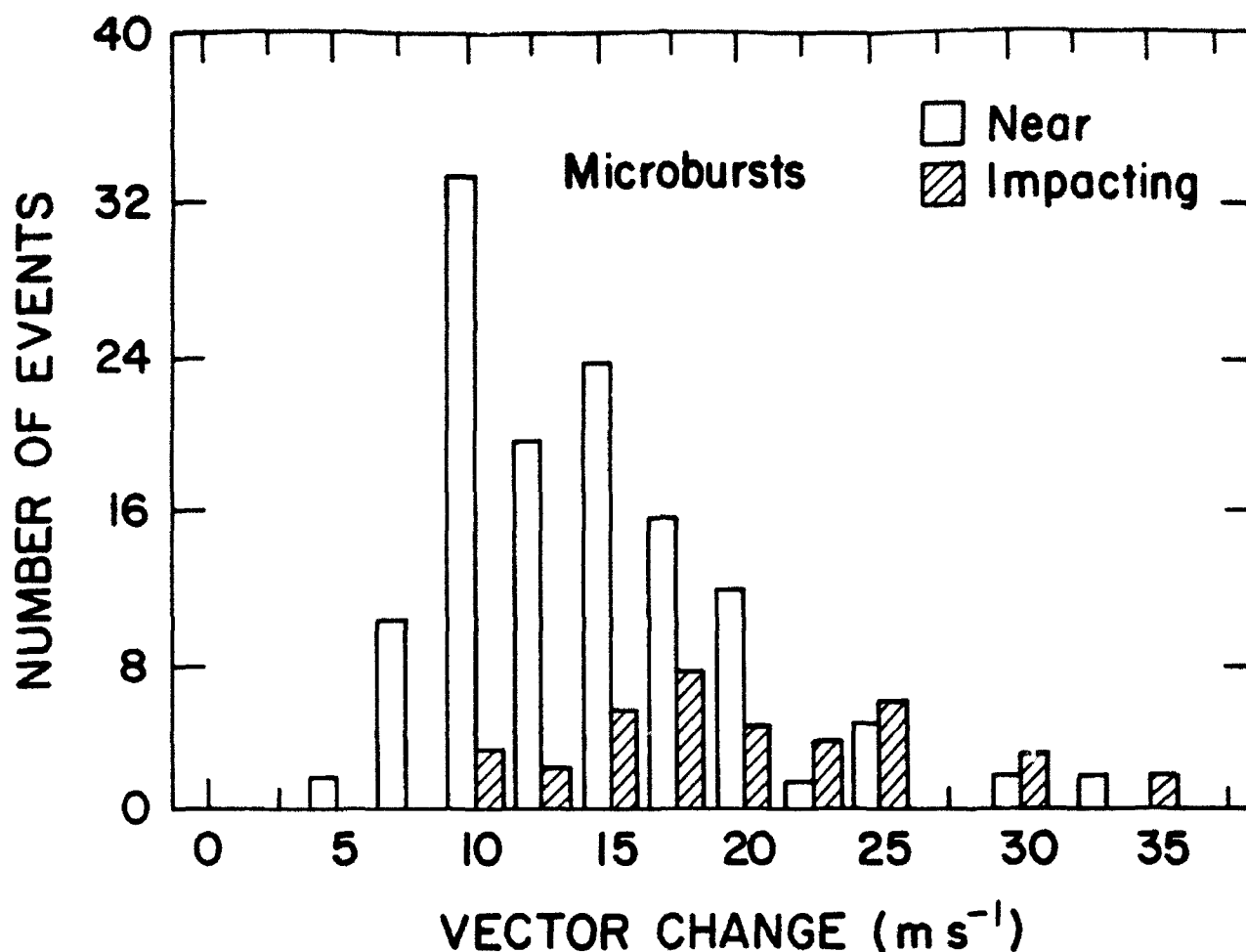
FIGURE 2.2. Similar to Fig. 2.1, this distribution shows the maximum wind vector change for impacting and near microbursts. For the near microbursts, the distribution peak is near 10 m s^{-1}, and for the impacting microbursts, the distribution peak is near 17.5 m s^{-1}. This is not surprising, since the maximum vector change—almost equal speeds separated by 180°—is anticipated as a microburst passes directly over a station; the direction change will not be 180° if a microburst does not pass directly over a station.

TEMPERATURE CHANGE
ASSOCIATED WITH MICROBURSTS
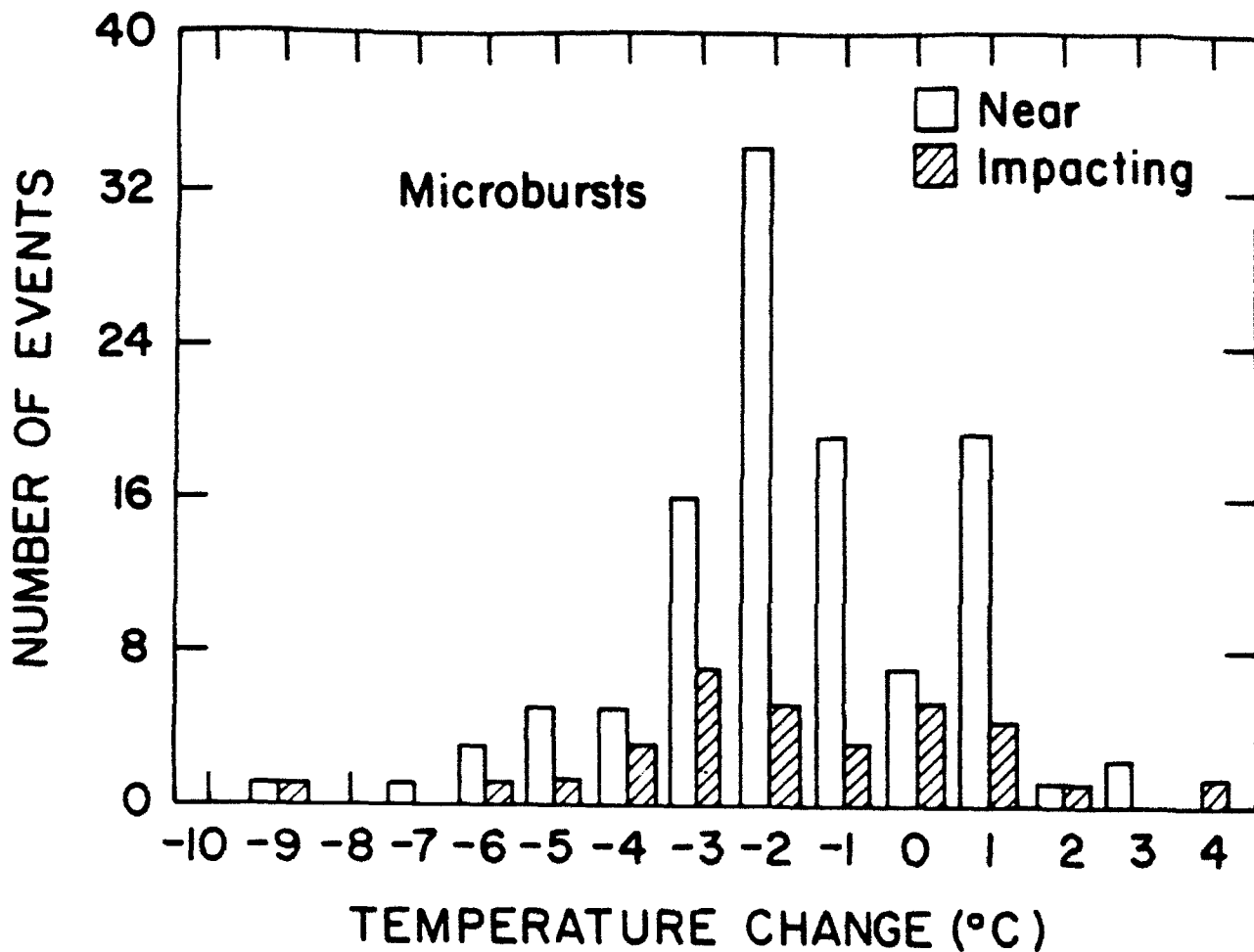
FIGURE 2.3. This is a frequency distribution for temperature change associated with impacting and near microbursts. The peak for the impacting microbursts is slightly cooler than for the near microbursts, which is expected since turbulent mixing has a chance to play more of a role in the near cases than in the impacting cases.

PRESSURE CHANGES ASSOCIATED WITH MICROBURSTS
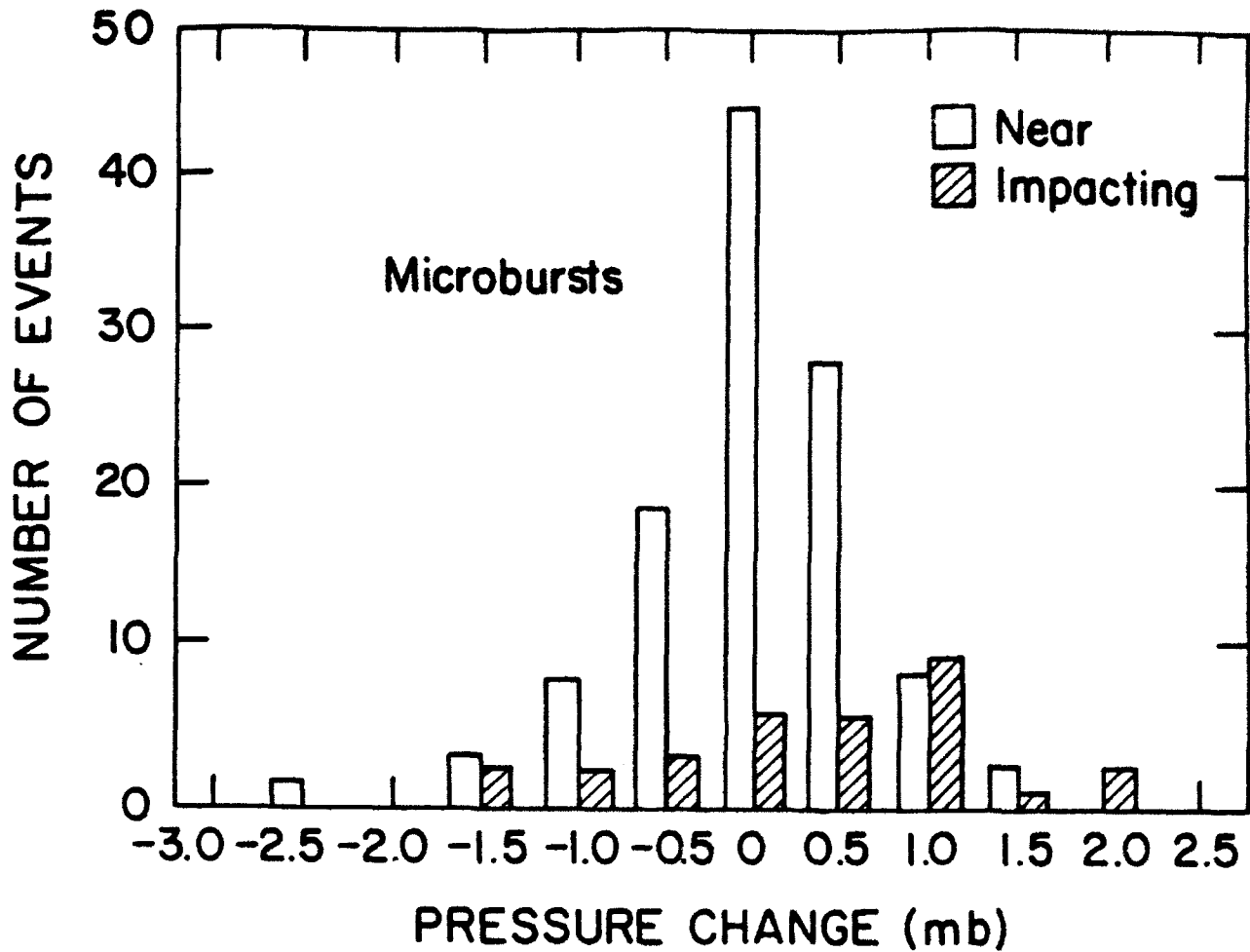
FIGURE 2.4 The pressure change frequency distributions are shown in Fig. 2.4. The impacting distribution shows a definite skew towards pressure rises, while the near distribution is less skewed. Again, this is expected because the center of the microburst should have the highest pressure, hydrostatically.

MIXED-LAYER LAPSE RATE
ON MICROBURST DAYS
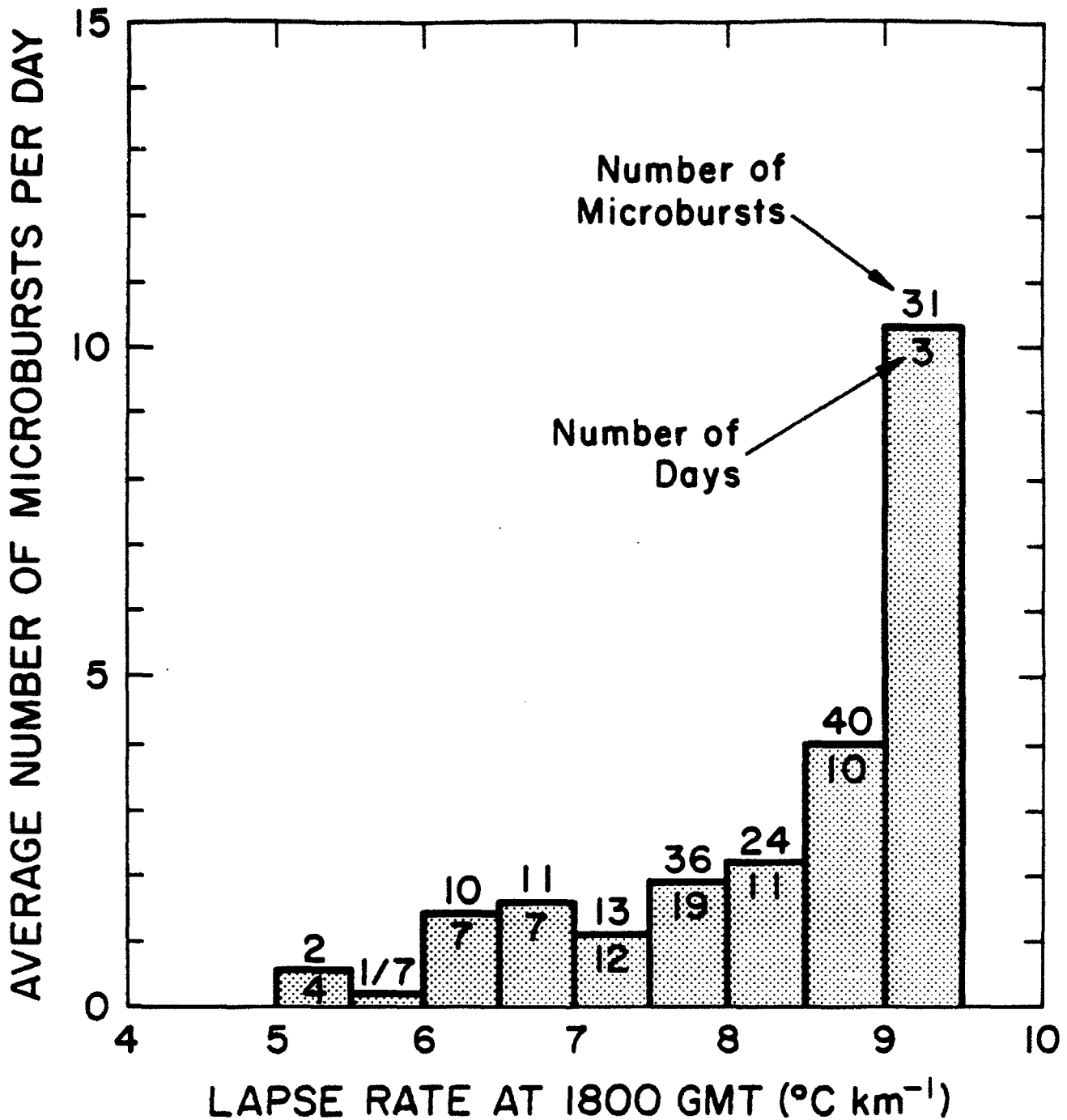
FIGURE 2.5. This figure represents a frequency distribution of the average number of microbursts occurring per day as function of the lapse rate in the boundary layer for the 18Z sounding. This distribution shows that microbursts are much more likely as the boundary layer lapse rate approaches dry-adiabatic, i.e., a neutrally stable boundary layer. A dry-adiabatic lapse rate means that any convectively-driven downdraft will continue downward without inhibition by static stability. If the boundary layer lapse rate is less than dry-adiabatic, downdrafts will tend to decelerate as they proceed toward the ground.

9

MICROBURST PRESSURE CHANGES VS. MAXIMUM WIND SPEED CHANGES
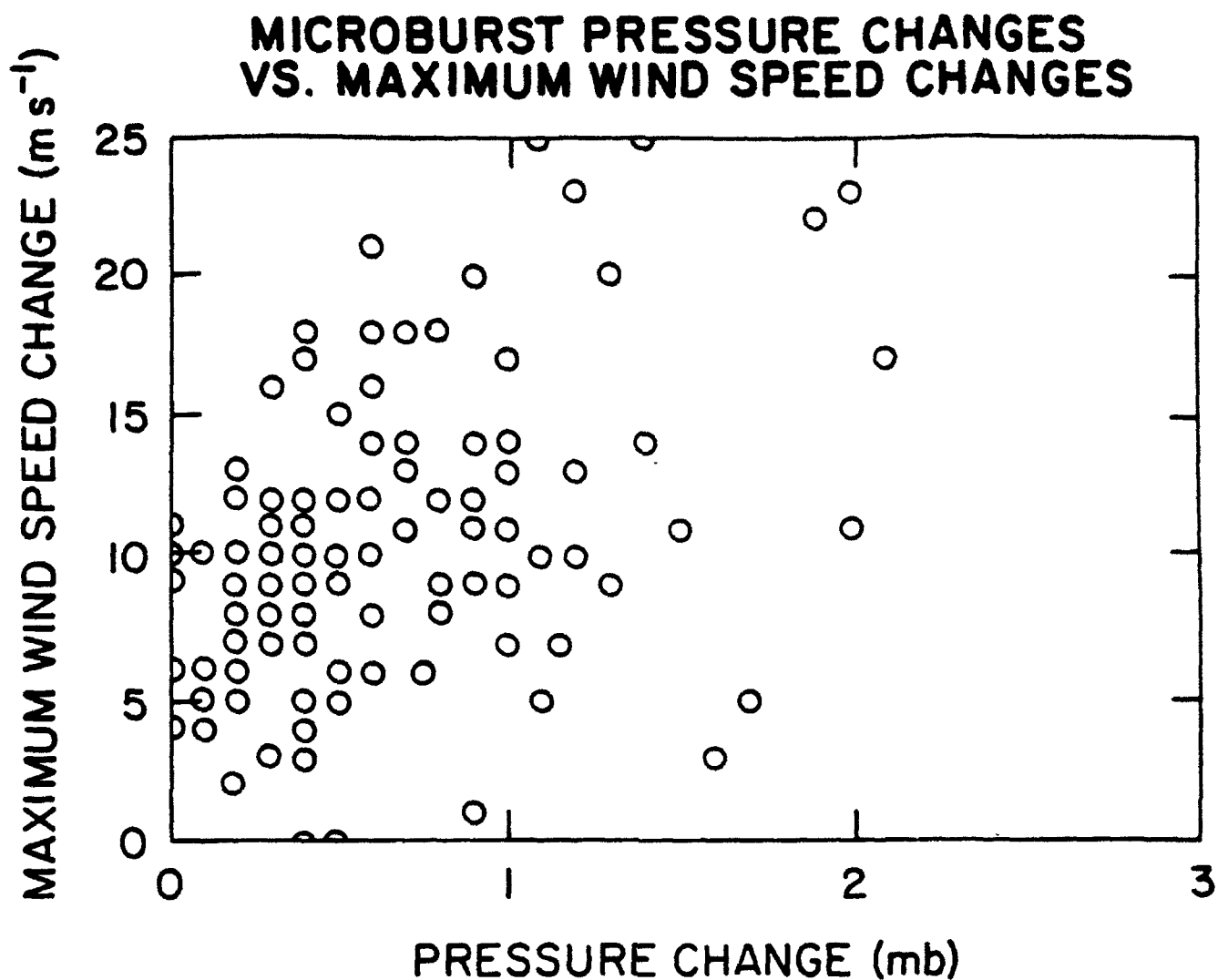
FIGURE 2.6. This figure is for a single PAM station and shows the maximum wind speed change as a function of pressure change for all cases where pressure increased. This figure is for all microbursts identified as affecting the station. There is no significant correlation between the two.

10

MICROBURST TEMPERATURE CHANGES VS. MAXIMUM WIND VECTOR CHANGE
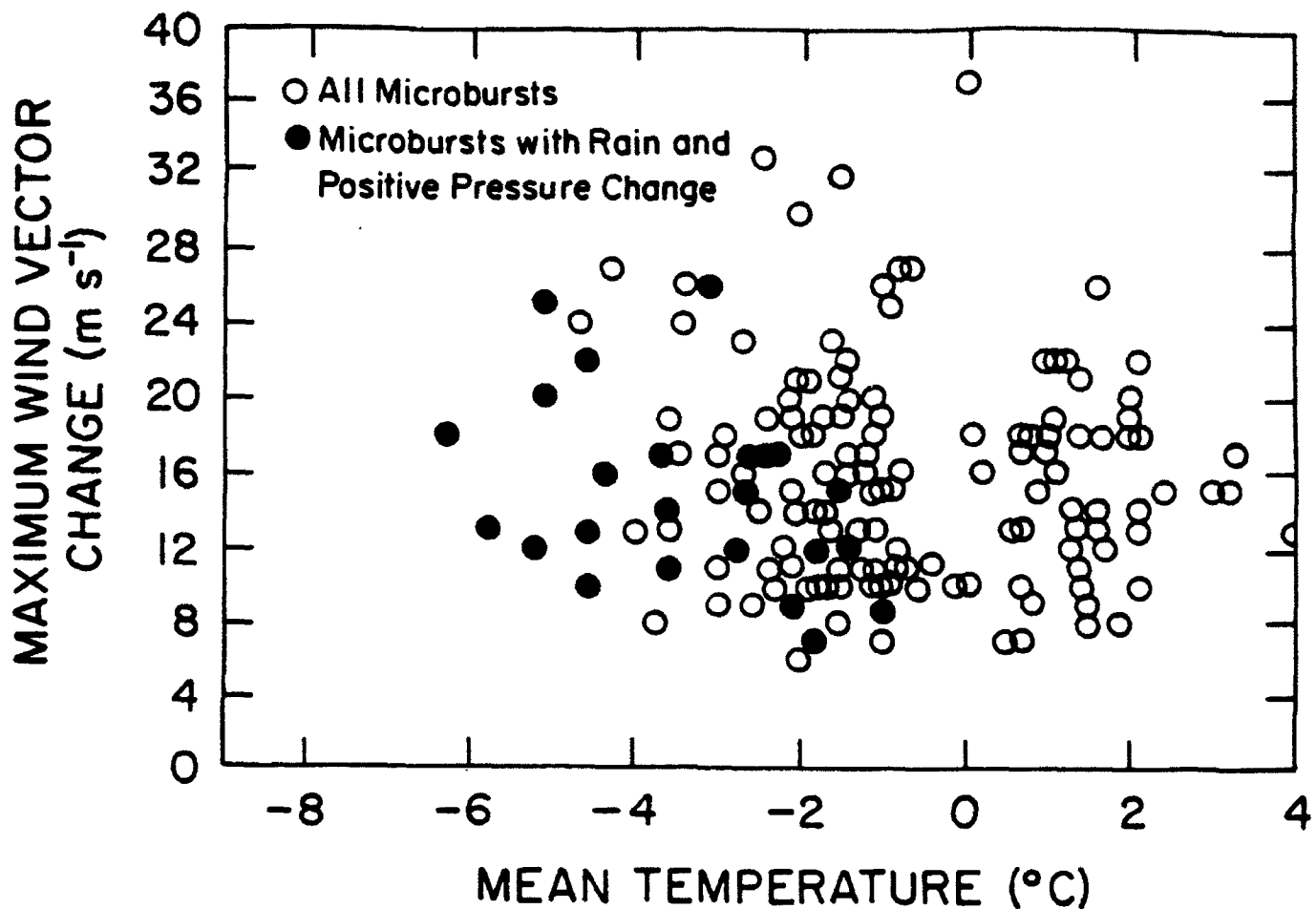
FIGURE 2.7. Figure 2.7 is similar to Fig. 2.6, except the mean wind vector change is plotted as a function of temperature change. The black dots show those cases where rain and a positive pressure change are associated with the event. There is no clear correlation between wind vector change and temperature change, even when rain and a positive pressure change are present.
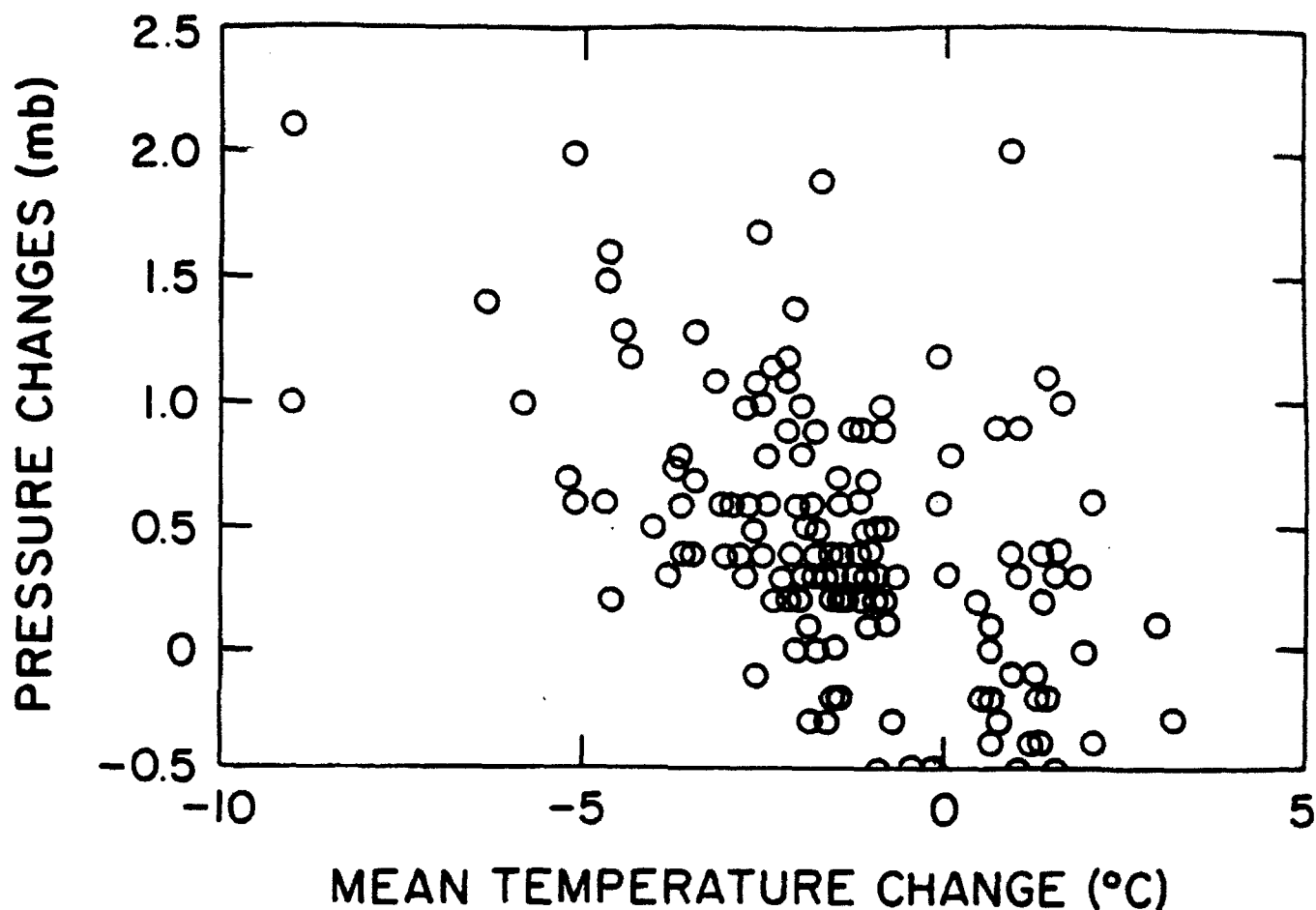
FIGURE 2.8. This figure shows the maximum pressure change as a function of mean temperature change for all PAM stations that were affected by all microbursts. There is a general tendency for pressure increases to be associated with temperature decreases, but no clear correlation.

MICROBURST PRESSURE CHANGE VS. MAXIMUM WIND SPEED CHANGE
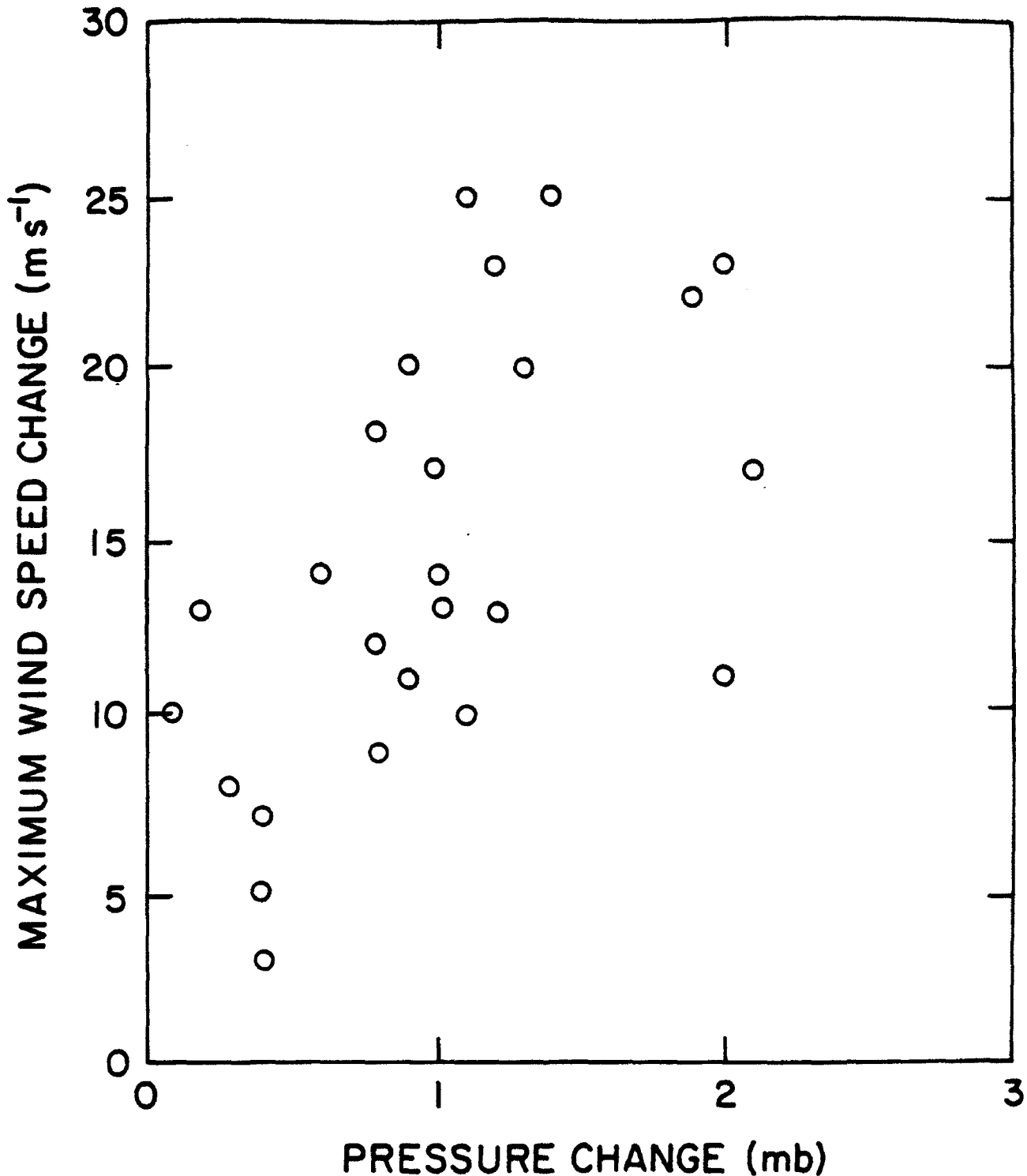
FIGURE 2.9. This figure is identical to Fig. 2.8 for impacting microbursts, only. In this data set, there is a correlation between pressure change and maximum observed wind speed change. If a mature microburst passes directly over a pressure sensor, the maximum wind speed change associated with it can be determined with some certainty.

13

TIME SERIES OF PRESSURE AND VECTOR WIND CHANGES FOR SELECTED MICROBURSTS
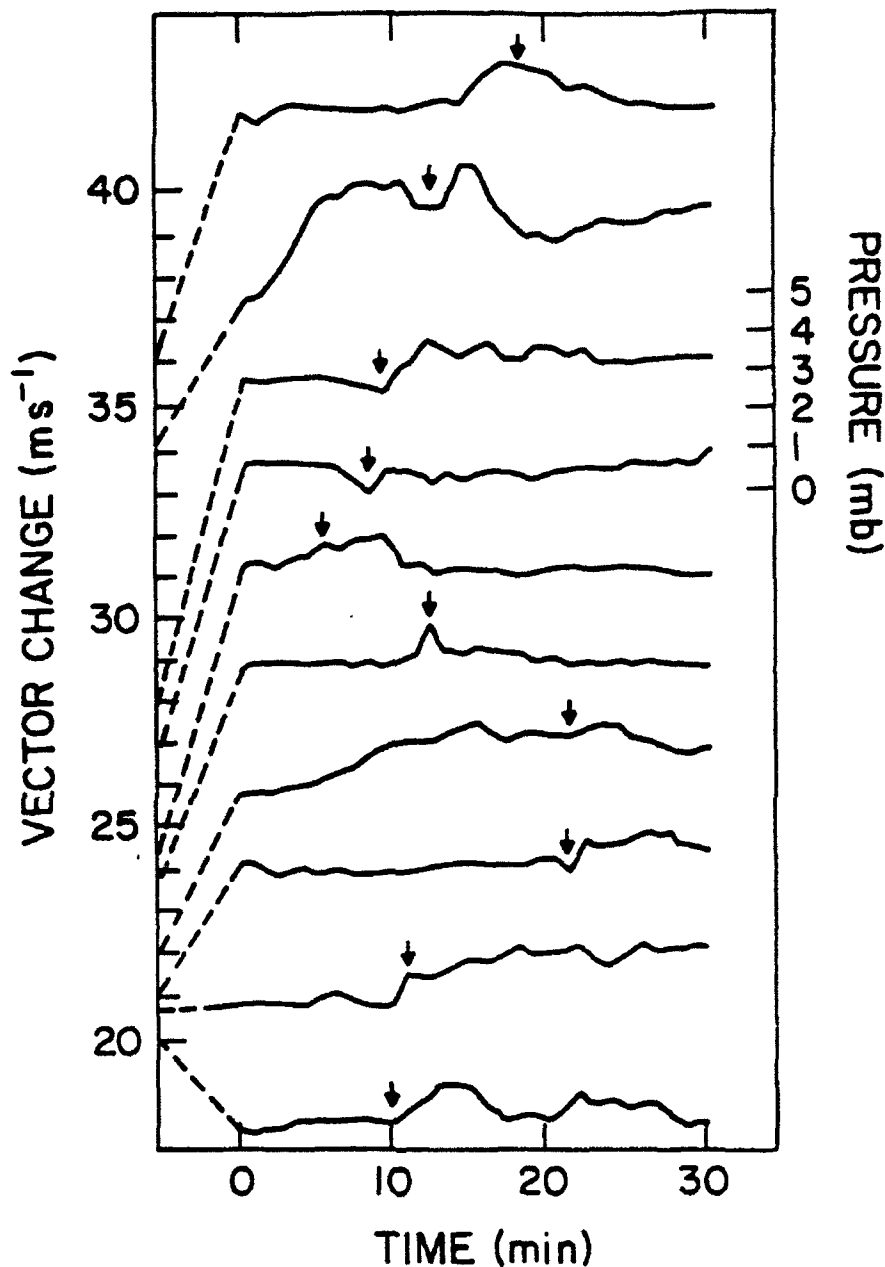
FIGURE 2.10. This figure is provided as a final example of how complex and unique each microburst event is. It shows a pressure time series for ten separate events that passed directly over a station, all associated with wind vector changes of 20 m s^{-1} or greater. The pressure scale is shown at the right, and the terminus of the dotted line on the left-hand scale shows the maximum wind vector change for each event. The arrows point to times of maximum wind speeds. Clearly, the time of maximum wind speed is not associated with any particular pressure signature—it can occur at pressure peaks, valleys, or in relatively quiescent pressure periods.

14

3. Radar-Derived General Statistics

During JAWS, the radars were active for limited periods, typically between about 1200 and 2000 MDT, depending upon when convective activity in the area ceased. For this reason alone, the radar-derived statistics represent an incomplete database when compared to the PAM data.

It must also be borne in mind that the JAWS radars often scanned only limited sectors; the entire region was not necessarily observed by radars at all times. This is quite unlike the PAM network, all of which was active 24 hrs a day. Often, a storm was scanned after the first signs of an outflow were observed. Occasionally, a storm was scanned well before any outflow was apparent. In some instances, a storm that never produced an outflow was scanned for an extended period of time, in hopes of observing a nascent outflow, while other storms produced outflows that were missed. Certain storms known to produce outflows have not been included because they were too far away. Data on low-altitude outflows become unreliable at long ranges (more than 40–60 km) due to terrain effects and uncertainties about the radar beam location.

DISTRIBUTION OF MICROBURST
OCCURRENCE RELATIVE TO TIME OF DAY
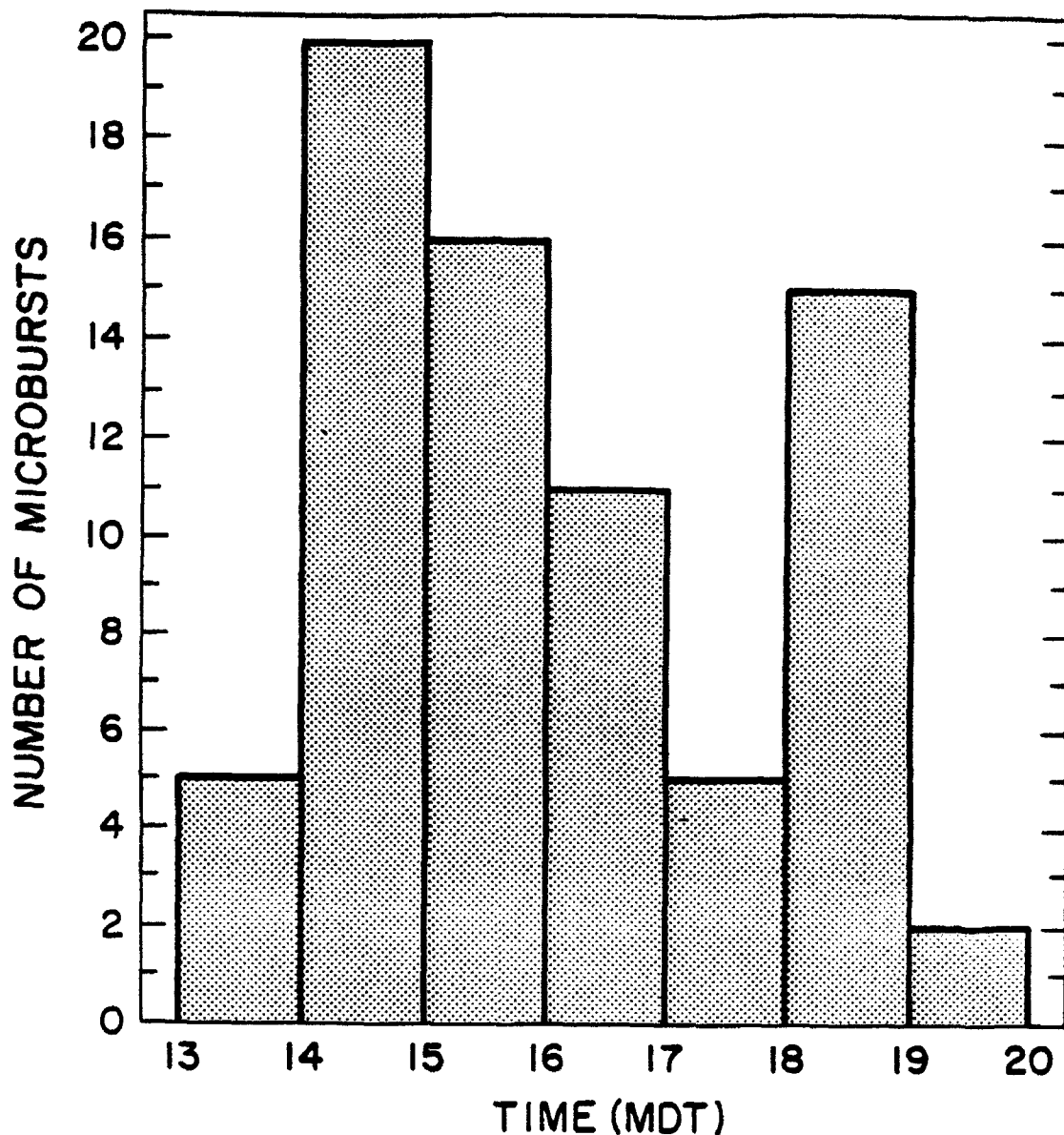
FIGURE 3.1. Microbursts are clearly associated with convective activity. This figure shows the average distribution of microburst occurrences within each hour. Peak occurrence between 1400 and 1600 MDT is associated with a peak in convective activity driven almost exclusively by insolation. A sharp secondary peak occurs between 1800 and 1900 MDT. Convection forming early in the day will reduce insolative heating and create mild subsidence in the area, suppressing any new convective formation. However, as the previous convection dissipates and/or moves eastward, solar heating again becomes important. In addition, outflow boundaries from the previous convection are still active. Thus, convection is initiated a second time by a combination of additional insolation and convergence associated with old convective outflow boundaries (Wilson et al., 1984).

DISTRIBUTION OF ΔV FOR JAWS (Only) MICROBURSTS AT 0° ELEVATION ANGLE
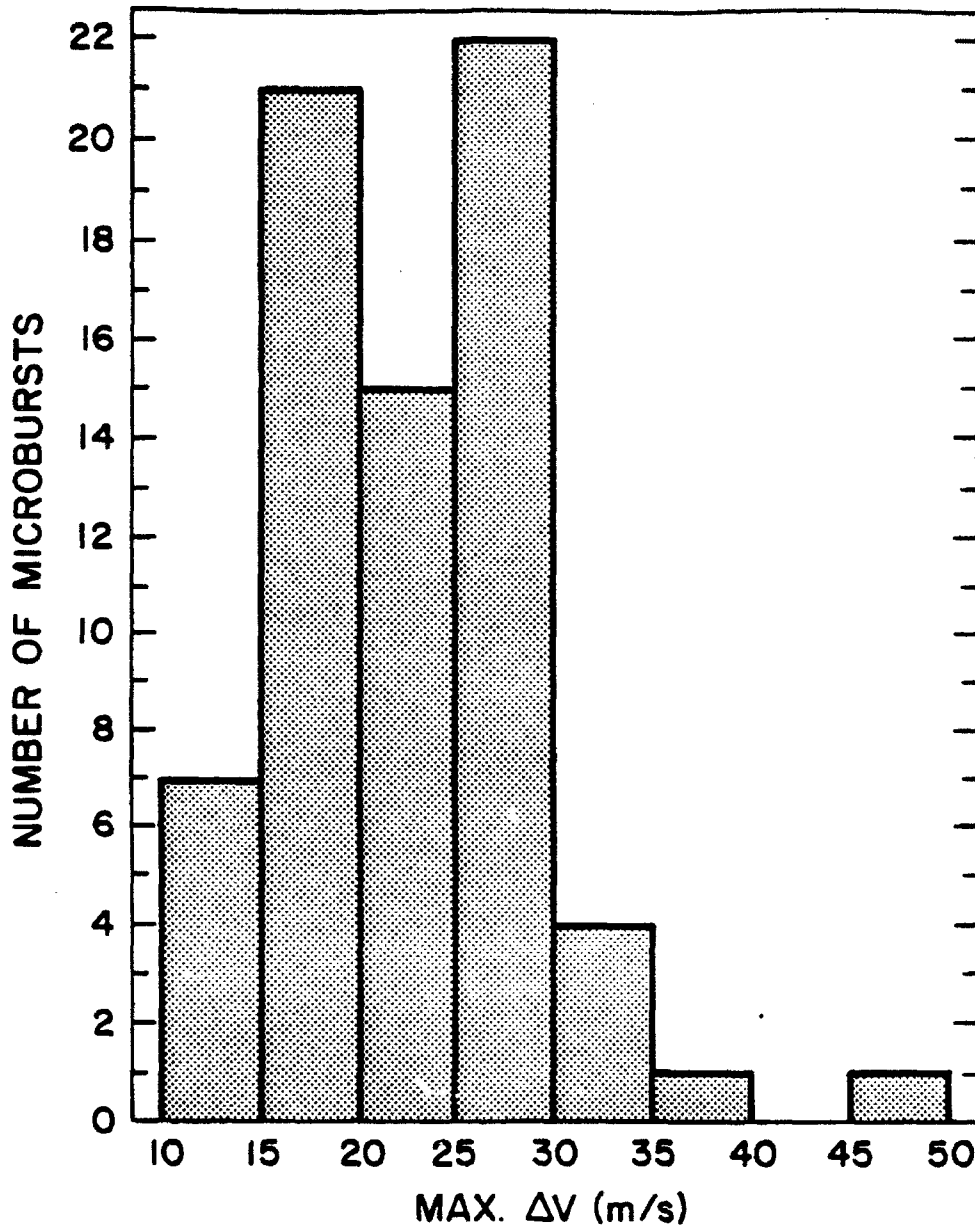
FIGURE 3.2. The distribution of maximum ΔV_r plotted vs the number of microbursts is shown in Fig. 3.2. Seventy-one samples comprise this distribution, some of which are samples of the same event taken during various stages. ΔV_r is the difference in velocity across the microburst, i.e., the difference between the maximum approaching and receding velocities viewed by a single-Doppler radar. These data were taken from the 0° elevation at a range of 60 km or less. Almost all events were within 50 km, so neglecting terrain variations, the effective height of the radar beam above the earth is between several meters and approximately 300 m. A later figure will discuss the measurement height distribution. The mean of the distribution is 24 m s^{-1}. Most microbursts display a ΔV_r between 15 and 30 m s^{-1}, although very strong events did occur (Wilson et al., 1984).

NUMBER OF MICROBURSTS OCCURRING PER DAY
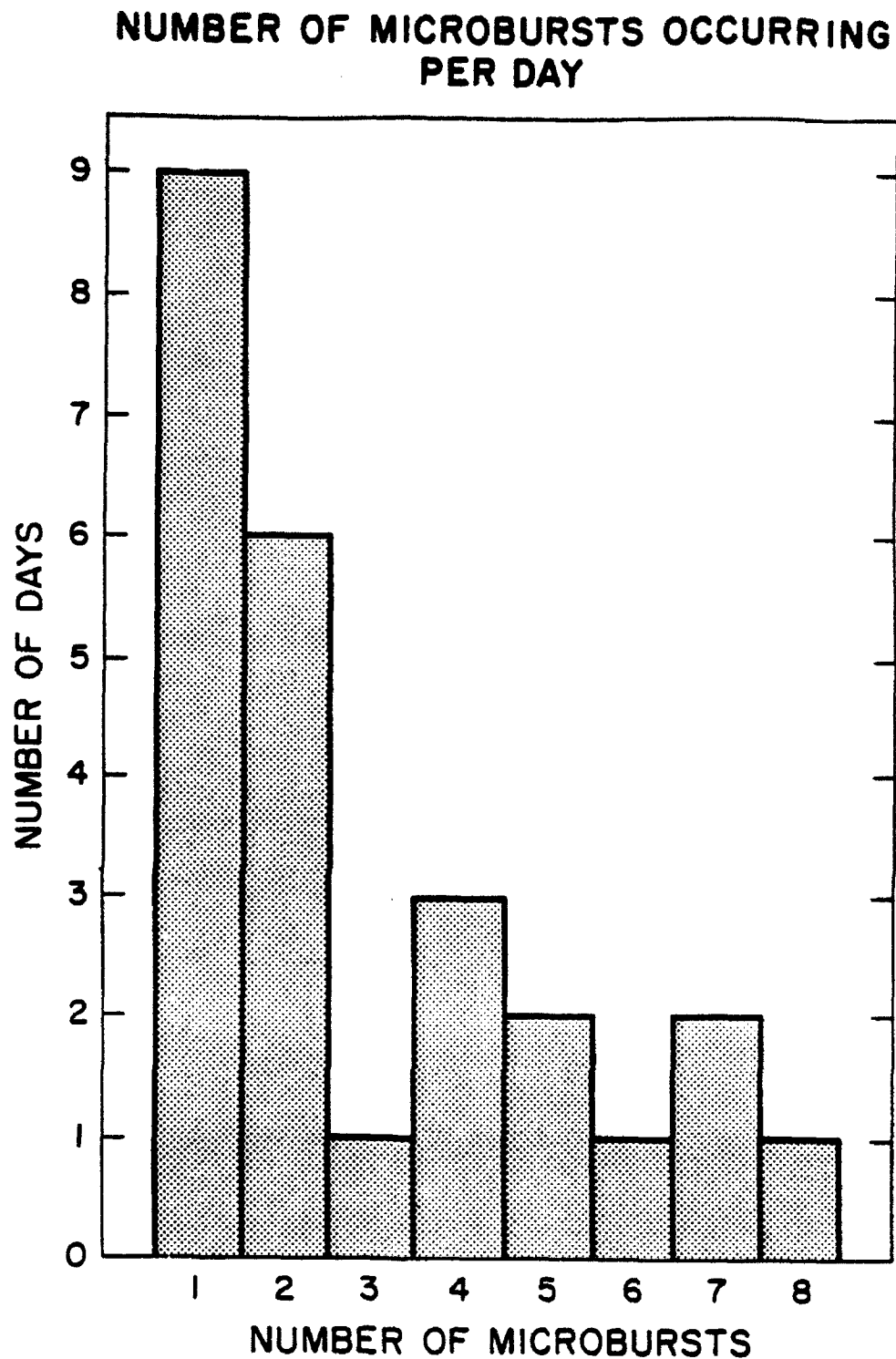
FIGURE 3.3. This figure shows the frequency distribution for the number of microbursts occurring per day. Studies by Kessinger et al. (1986) indicate that microbursts typically occur in groups of two or more; of 25 days investigated, a single microburst occurred on only nine (36%) days. Although multiple microbursts may not be associated with a single storm, once a microburst has occurred, conditions are clearly conducive to others.

RADIAL SHEAR vs. DISTANCE
BETWEEN VELOCITY COUPLETS
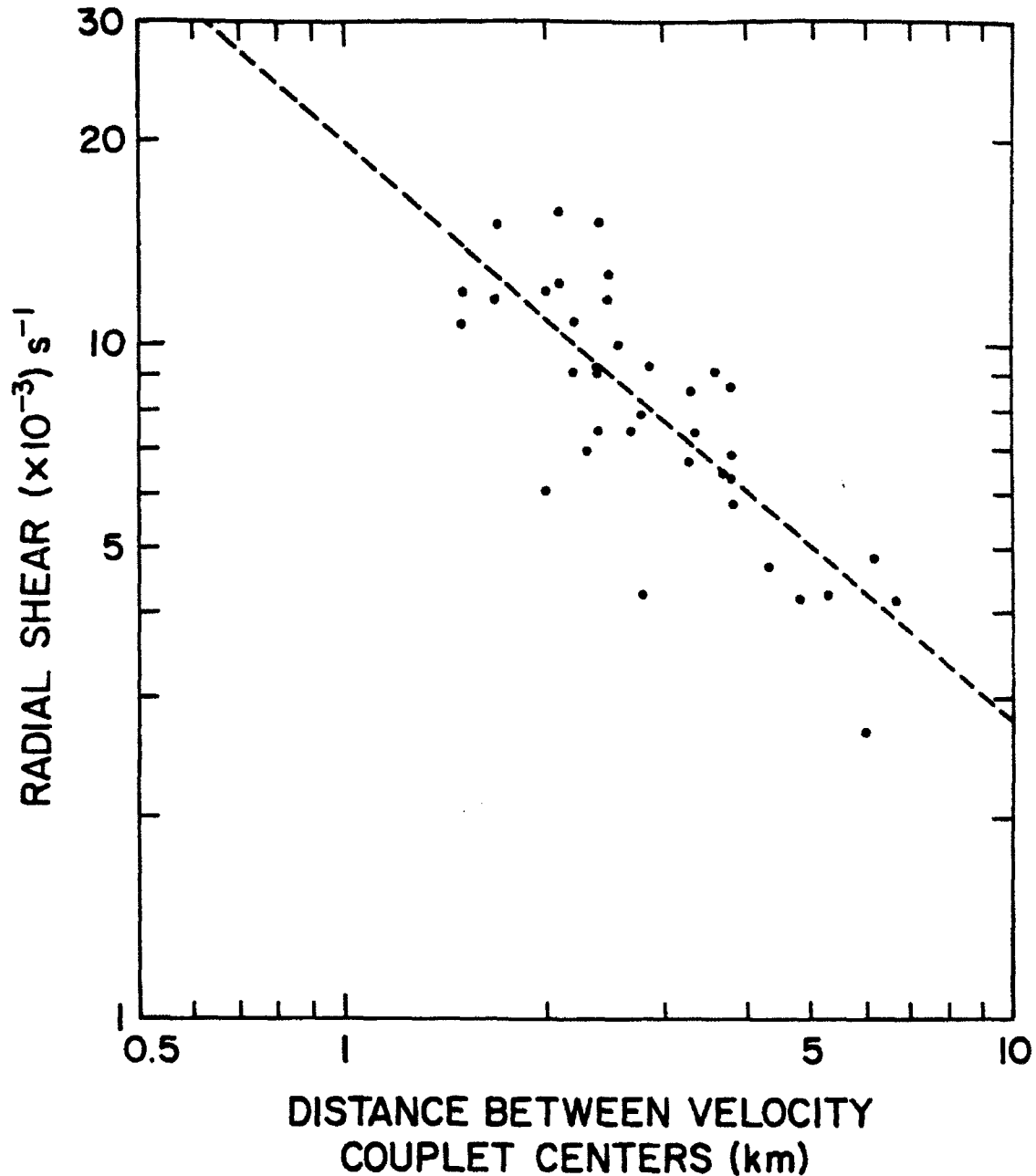
FIGURE 3.4. This plot is taken from data that appear in Table 2 of Wilson et al. (1984). The log of radial shear (in units of $\times 10^{-3}$ s^{-1}) is plotted against the log of the distance between the velocity couplets. The dashed line shows the linear least squares regression line that fits the data. The line has the form: $\ln y = \ln b + m \ln x$, where y is the radial shear and x is the distance between couplets. The power function represented by the line has the form: $y = bx^{m}$. Using a Student's-t distribution, the regression is significant at the 99.9% level. The shear is likely a function of the distance between velocity couplets, but no guarantees can be made about the parameters of the power function. For this fit, $m = -0.86$, $b = 7.45$, and the correlation coefficient $r = -0.78$.

TIME TO MAX FOR MICROBURSTS
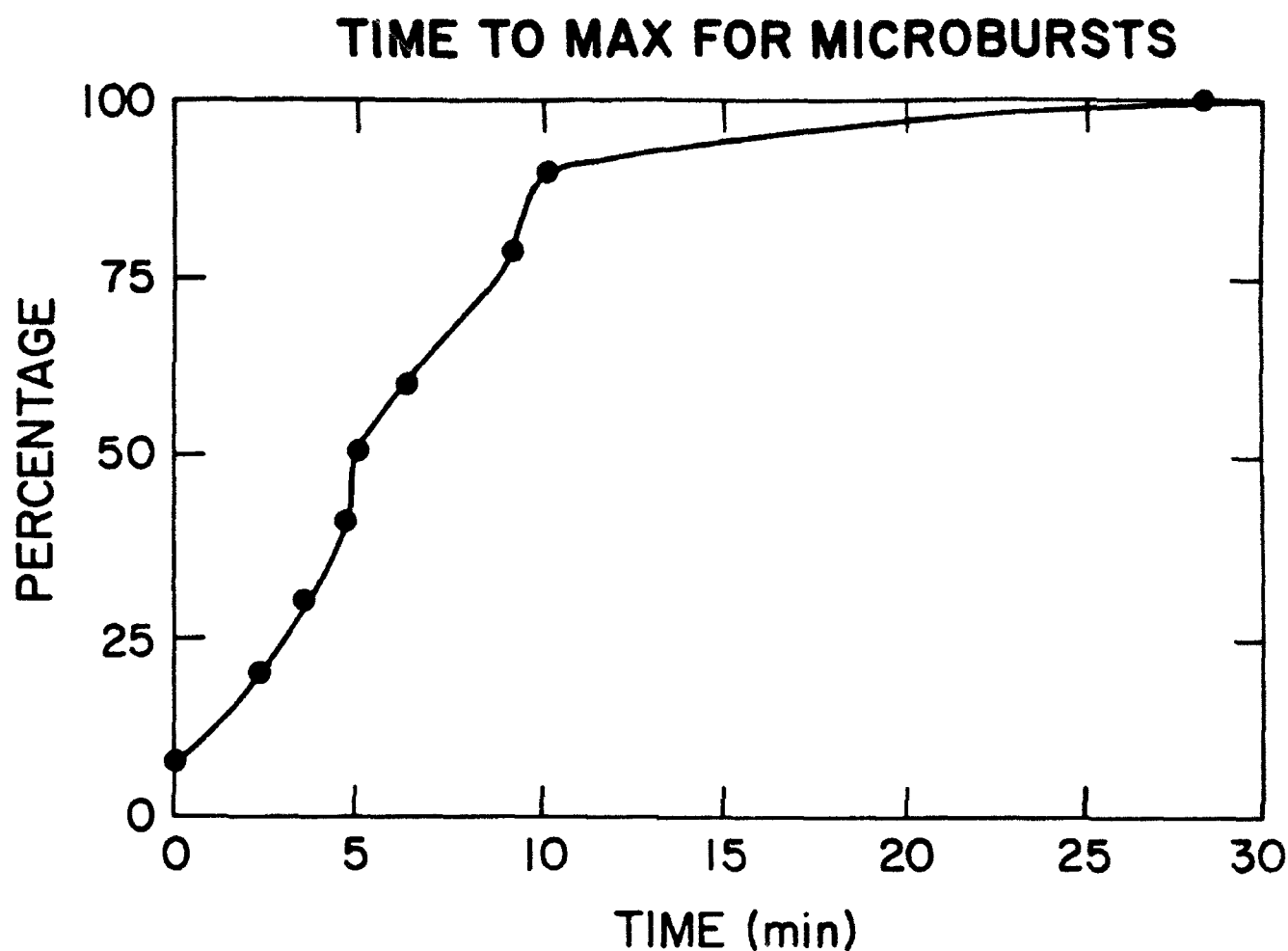
FIGURE 3.5. Microbursts are transient events that change rapidly. Figure 3.5 shows the percentage of microbursts that reach maximum strength within a given time. Due to the update rate used in JAWS and CLAWS, some microbursts formed and reached maximum strength between the 2-min scans. Fifty percent of the microbursts examined reached maximum strength in 5 min. Within 10 min almost 90% had reached maximum strength, while one event required 28 min to reach full strength. A small number, about 10% , formed and reached the maximum observed strength in less than 2 min. A minimum scan interval should therefore not exceed 2 min.

4. Radar-Derived Statistics Associated With Velocity Maxima

This section focuses on a particular part of microburst outflows: the area of maximum wind speed, or velocity maxima. Each microburst has two velocity maxima as viewed by a single-Doppler radar, one approaching the radar and one receding from it. It is important to collect statistics on the velocity maxima structure because this determines microburst "detectability." Since microburst velocity maxima can be somewhat separated from the main rainshaft, their radar reflectivities are often considerably lower than the reflectivity associated with the microburst center. In addition, the distribution of reflectivity across the microburst is often asymmetric; one velocity maximum may have a radar reflectivity 10–15 dB greater than the other. The lower range of velocity maxima reflectivity is particularly important; if both velocity maxima cannot be detected by a radar, it is impossible to quantify the microburst hazard. Such information may affect the required signal-to-noise ratio of a radar or make a particular ground-clutter rejection technique unacceptable.

The vertical structure in reflectivity is important because the effective center of the radar beam may be as high as 100 m above the terrain. Should the reflectivity within the velocity maxima increase with height, it may be possible to develop a scan strategy that maximizes the probability of detecting both maxima and that also minimizes ground-clutter problems. On the other hand, if the reflectivities within the velocity maxima decrease rapidly with increasing height above ground level, antenna pattern and ground-clutter rejection techniques may become even more important.

LOWEST REFLECTIVITY OF MICROBURST VELOCITY MAXIMA 0 TO 100 m AGL
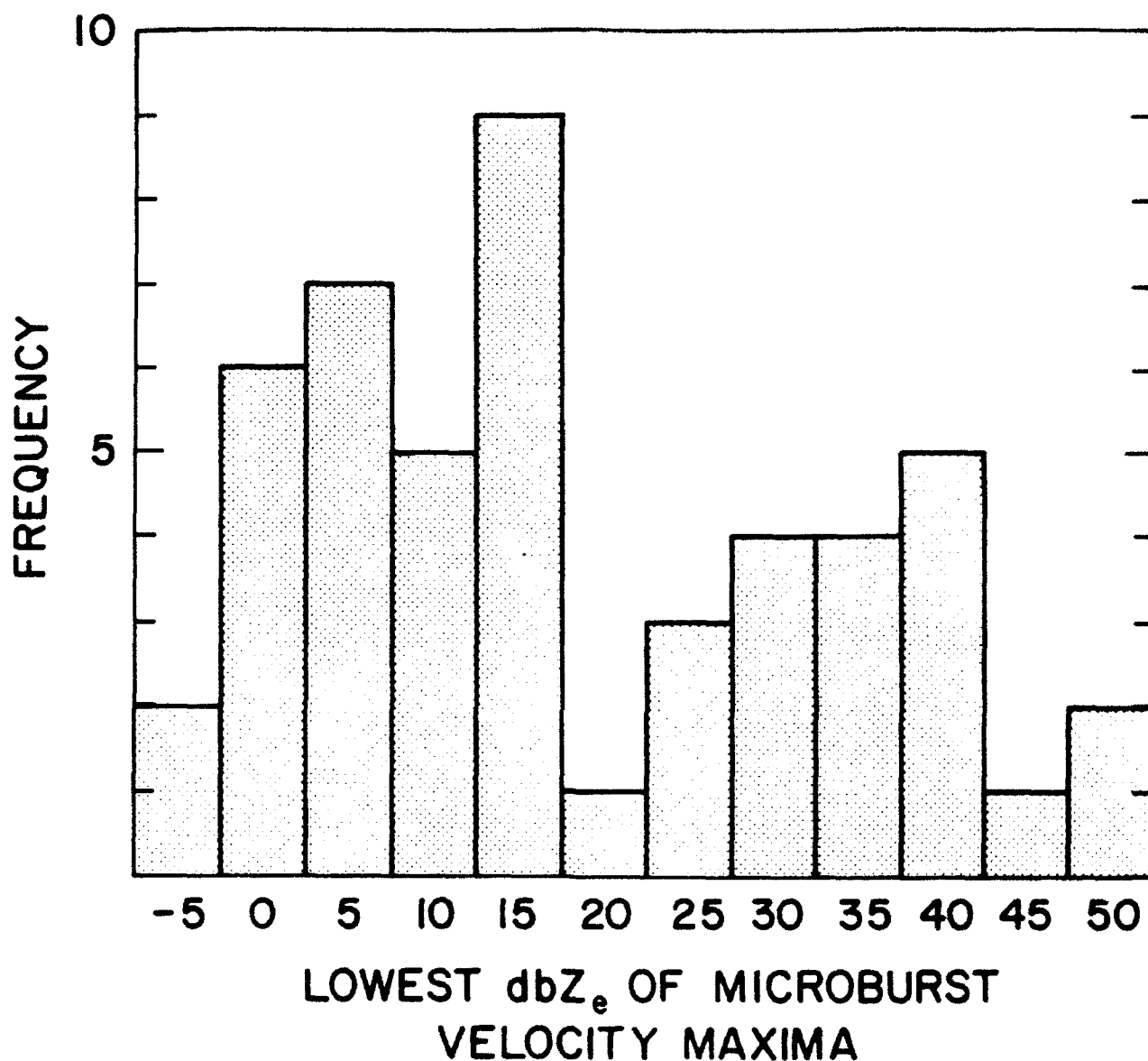
FIGURE 4.1. Under the supposition that both velocity maxima must be detected before quantitative information about the strength of a microburst event can be determined, the distribution of the lowest reflectivities of the microburst velocity maxima was examined. Figure 4.1 shows this distribution for heights between 0 and 100 m AGL. Of the 49 separate microbursts that make up the sample space, 15 (30.6%) possessed a reflectivity of less than 10 dBZ_e. The mean reflectivity for the receding velocity maxima is 22.1 dBZ_e, for the approaching maxima it is 24.3 dBZ_e and the average for the two is 23.2 dBZ_e. However, for the velocity maxima showing the weakest reflectivities, regardless of whether they are receding or approaching, the mean is 18.8 dBZ_e, with a standard deviation of 15.4 dBZ_e.

LOWEST REFLECTIVITY OF MICROBURST
VELOCITY MAXIMA 100-200m AGL
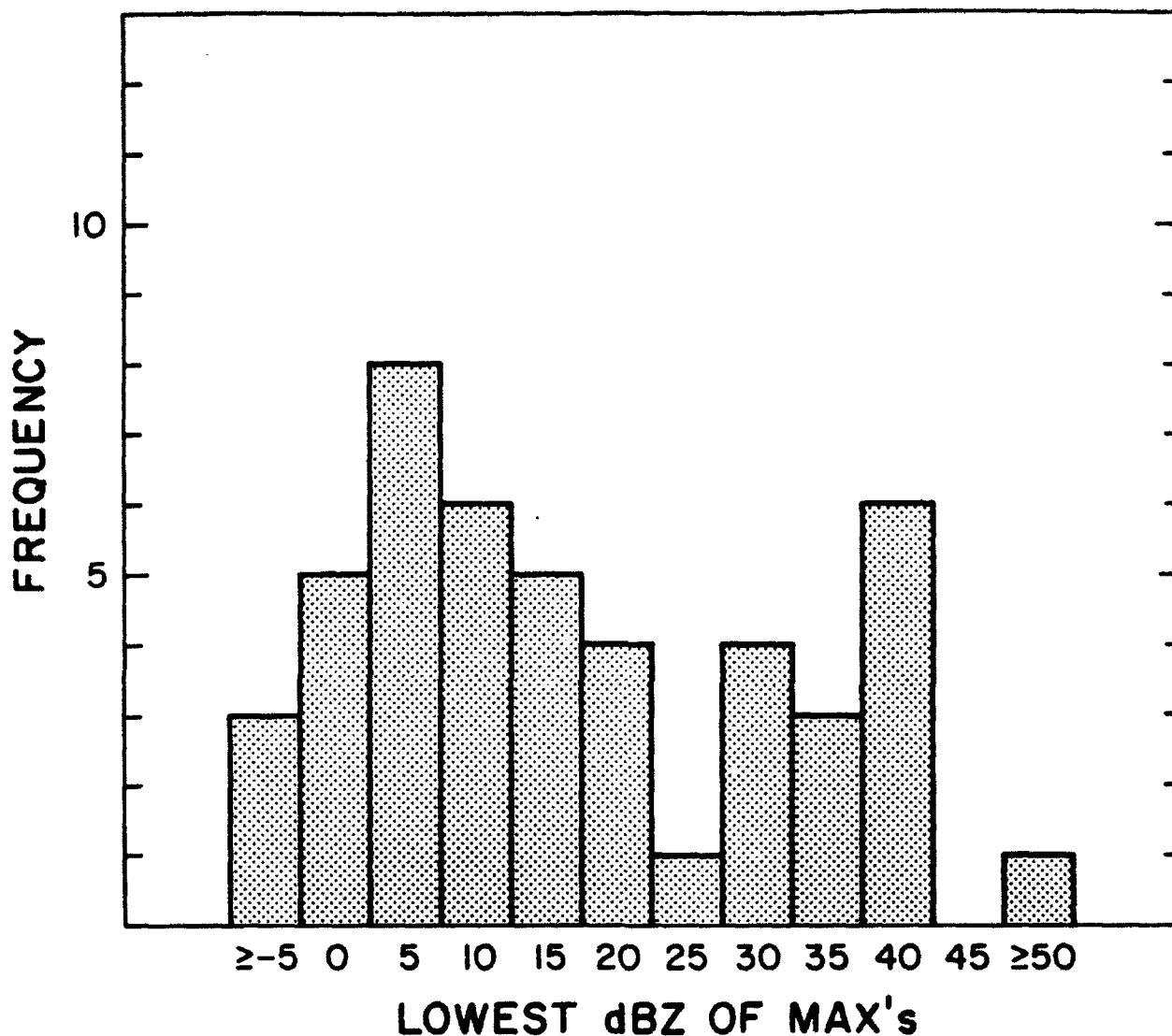
FIGURE 4.2. This figure is similar to Fig. 4.1 for heights between 100 and 200 m AGL. Of 46 microbursts comprising the sample space, 16 (34.8%) possess at least one velocity maximum with a reflectivity less than 10 dBZ_e. The statistics are almost identical: for the receding maxima, the mean reflectivity is 22.1 dBZ_e; for the approaching maxima, the mean is 24.0 dBZ_e; and for the maxima showing the weakest reflectivities, the mean is 19.0 dBZ_e, with a standard deviation of 15.5 dBZ_e. Statistically, there is no difference between this distribution and the one for heights between 0 and 100 m AGL.

LOWEST REFLECTIVITY OF MICROBURST VELOCITY MAXIMA 200-300 m AGL
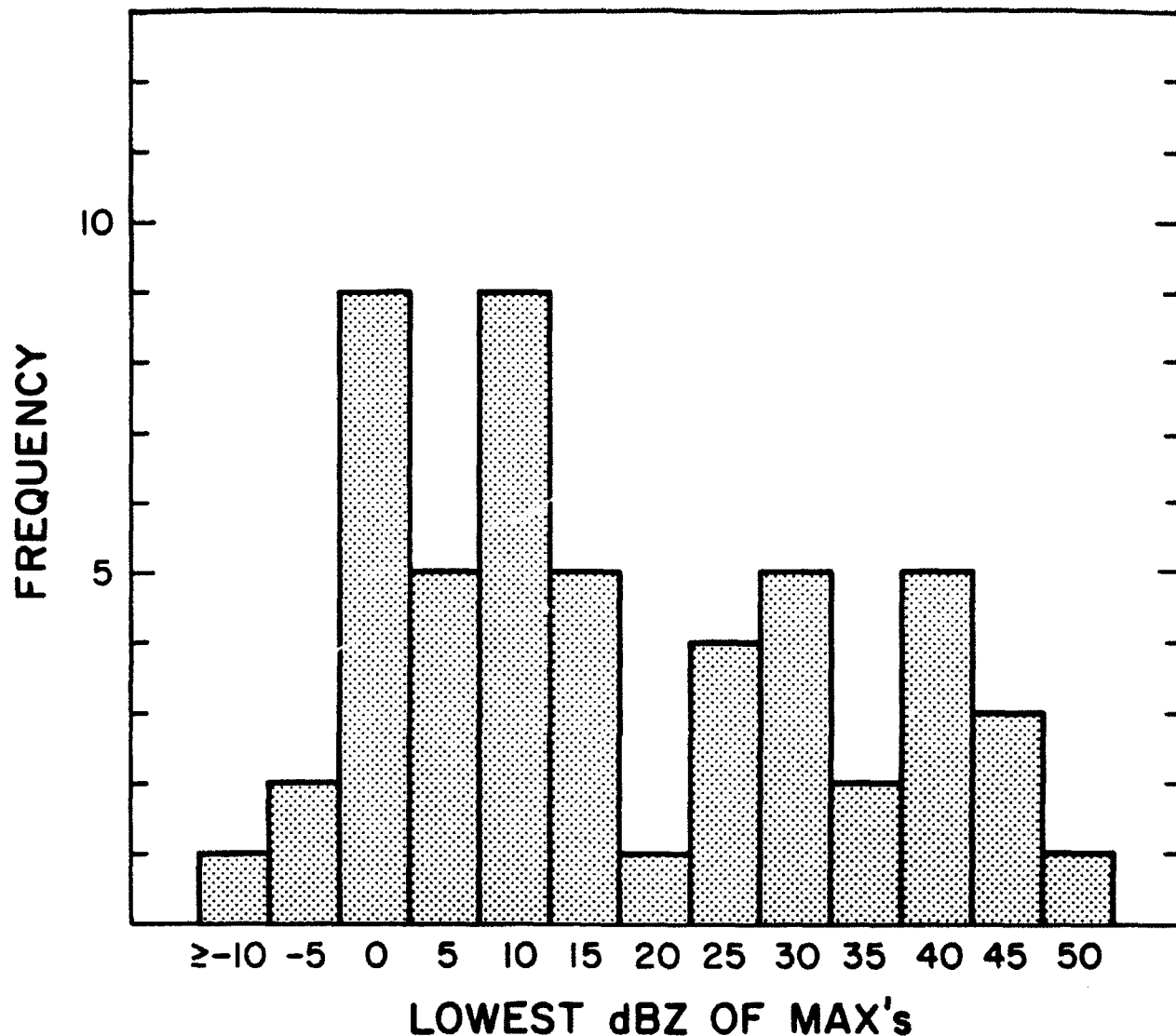
FIGURE 4.3. The same kind of distribution graphed in Figs. 4.1 and 4.2 is shown in Fig. 4.3 for heights between 200 and 300 m AGL. Fifty-one microbursts make up the sample space of this distribution. Thirty-three percent (17 events) have velocity maxima with associated reflectivities of less than 10 dBZ_e. As for the previous two distributions, the statistics are nearly identical: the receding maxima are associated with a 23.5 dBZ_e mean reflectivity, the approaching maxima with a 24.2 dBZ_e mean reflectivity, and the lowest maxima show a mean reflectivity of 19.7 dBZ_e, with a standard deviation of 15.7 dBZ_e.

The reflectivities within the velocity maxima neither increase nor decrease with height, at least for the first 300 m. Thus, if a radar is limited in its sensitivity, there is no benefit in viewing the storm at increased heights in hopes that more precipitation will exist slightly above the surface.
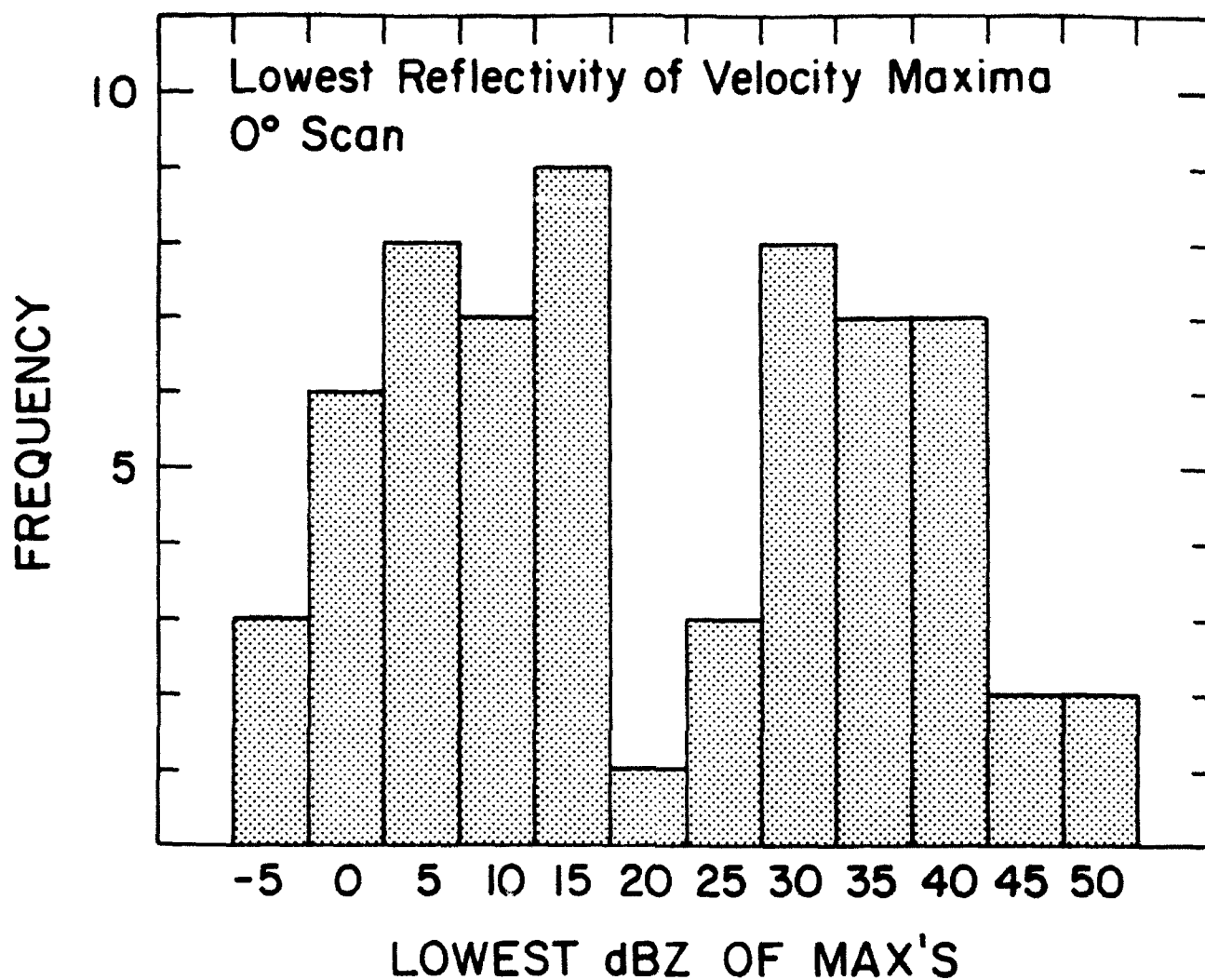
FIGURE 4.4. This figure is slightly different from the previous figures in that it shows the velocity maxima having the least reflectivities for 0° elevation scans. As expected from previous figures, the reflectivities of receding and approaching velocity maxima are 23.9 and 26.1 dBZ$_e$, respectively. The mean reflectivity of the lowest reflectivity velocity maxima is 20.5 dBZ$_e$, with a standard deviation of 16.6 dBZ$_e$. Of the 63 samples that are included in this distribution, 27% (17) possess reflectivities of less than 10 dBZ$_e$.

EFFECTIVE BEAM HEIGHT
FOR 0° ELEVATION ANGLE
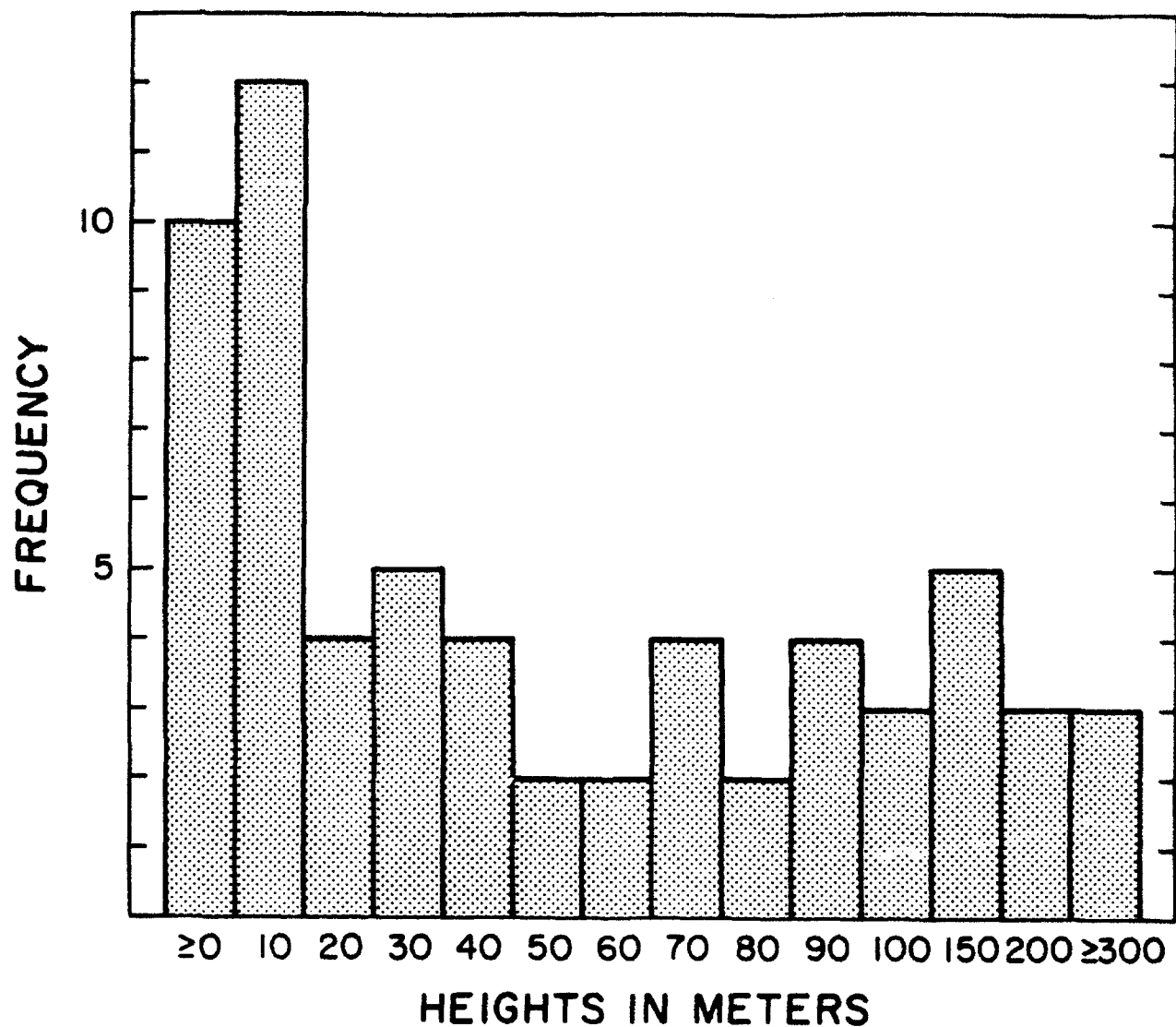
FIGURE 4.5. The height distribution for the 0° scans included in Fig. 4.4 is shown in this figure. Heights range from ~ 0–300+ m. The mean effective height of the radar beam above the surface, excluding terrain variations, is 75.5 m, with a standard deviation of 88.3 m.
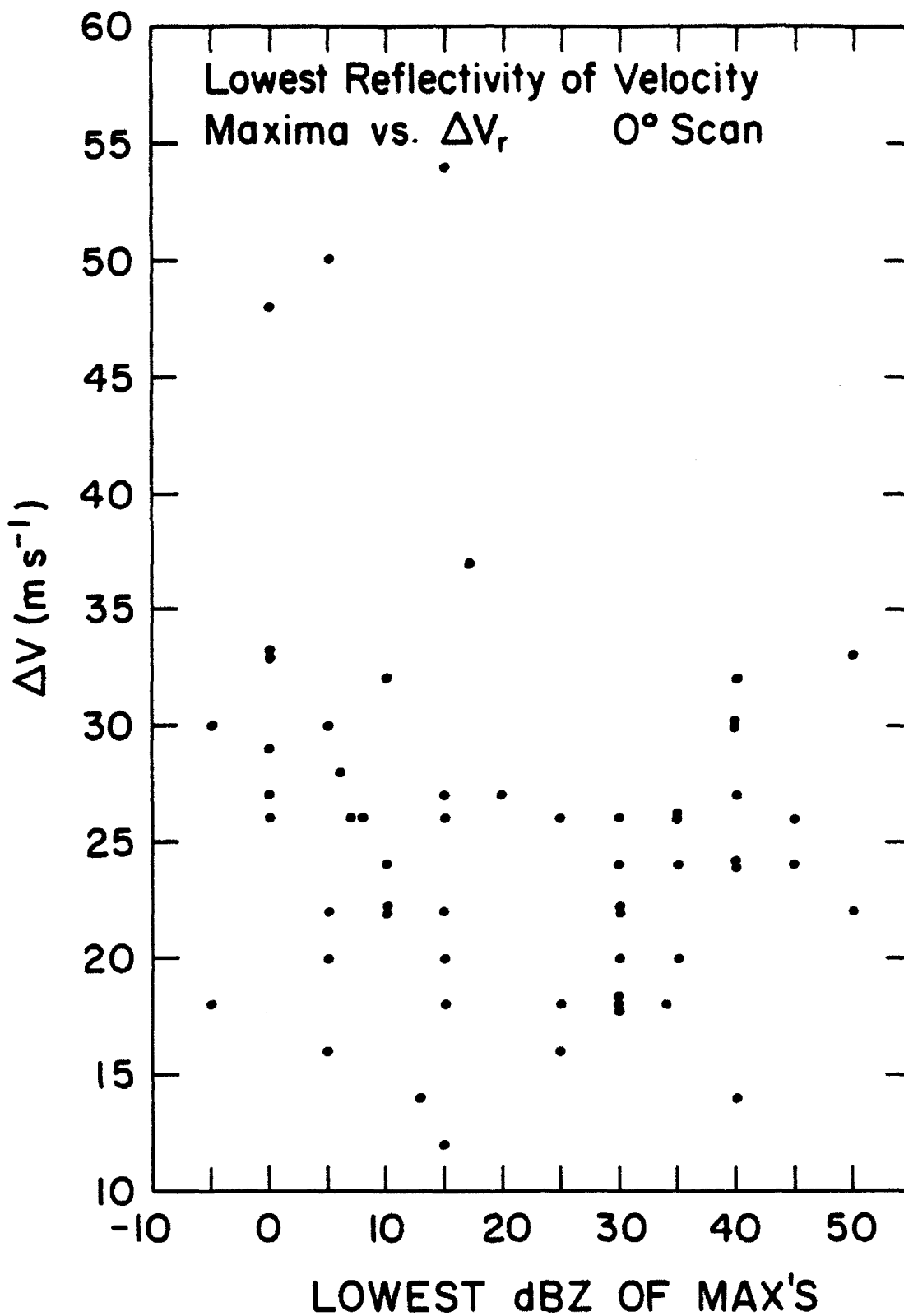
FIGURE 4.6. This scatter diagram is similar to Fig. 2.3, except for the lowest reflectivities of the two velocity maxima in the microburst. There are 63 microbursts included in this distribution. Just as for Fig. 2.3, there is no correlation between reflectivity and ΔV_r.

5. Radar-Derived, Small-Sample Characteristics

In a few cases, extremely detailed analyses in time and space have been performed on microbursts. These represent the best available data to date on microbursts. The cases for which this was done are special, not from a meteorological standpoint, but from a data standpoint—these are the only cases for which sufficient data were available to perform such analyses. Because the sample size is so small, typically less than ten cases, averages have little meaning. Nevertheless, common trends such as size growth as the outflow approaches maximum intensity can be identified. It is important to know the rate at which outflows intensify because this helps to determine the minimum lead-time required for a useful warning product. The velocity structure with height is useful, given some knowledge of the height of the radar beam, since primary interest is the outflow strength at or very near the surface where aircraft are most vulnerable. It may also determine the importance of antenna beam patterns and ground-clutter rejection methods.
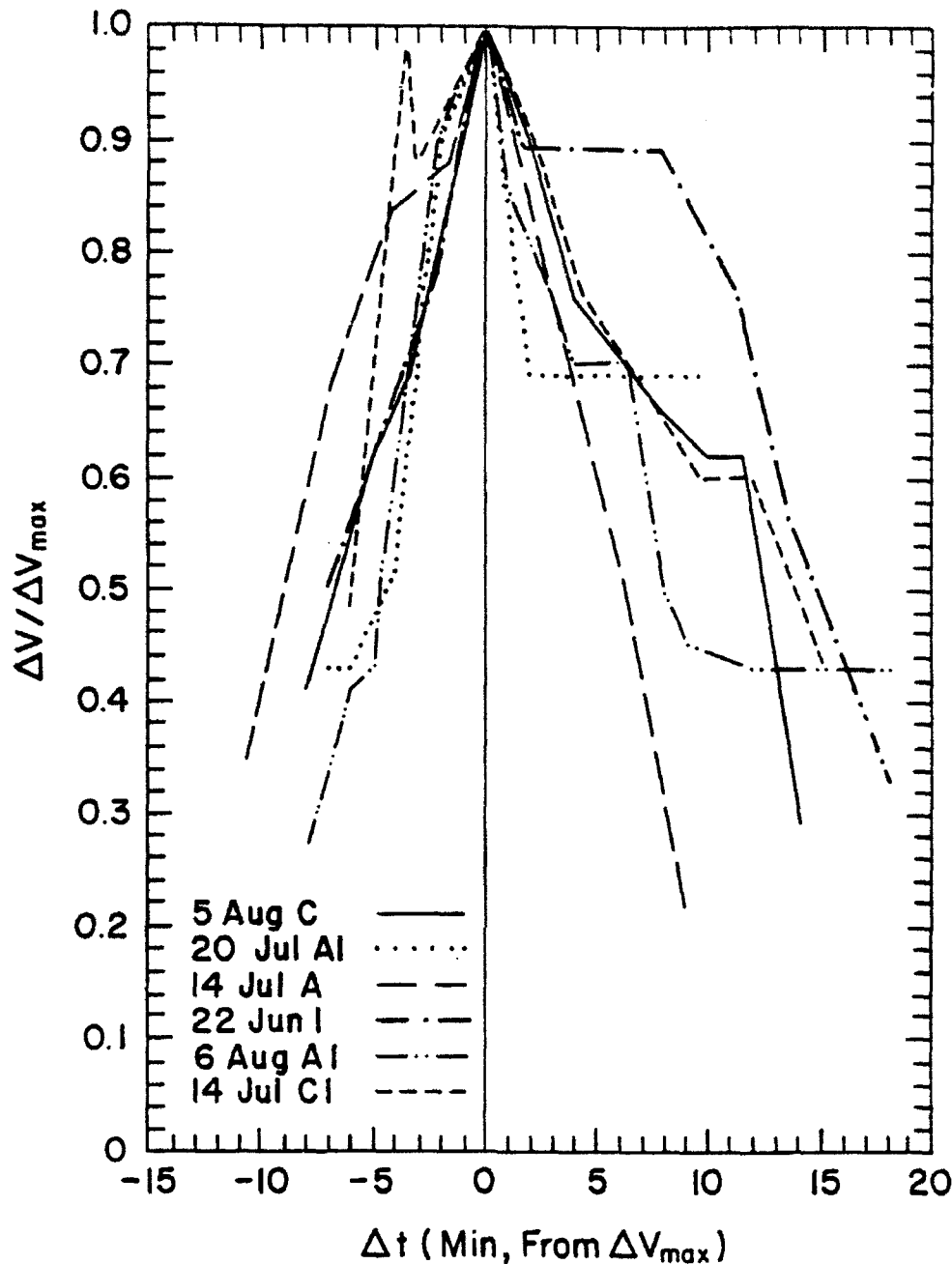
FIGURE 5.1. This figure shows the ΔV_r normalized to the maximum ΔV_r plotted against the time, in minutes, from the maximum ΔV_r for six microbursts. In general, microbursts tend to strengthen rapidly and decay somewhat slowly. (The rapid growth is illustrated in Fig. 2.6.) From this figure, it is evident that microbursts strengthen monotonically. However, microburst decay is not typically monotonic. While all microbursts in this small sample grew at similar rates in a similar fashion, the decay profile is different in each case. Most show steps, or plateaus, during their decay, but these plateaus occur at different times and strengths. Additionally, while the microbursts grew at very similar rates, the decay rates are quite different. This means that once a microburst initiates, it will steadily grow at a relatively predictable rate, but its decay is not as predictable. The time required for the microbursts to decay to some fraction of their maximum strength will not be similar from case to case.

DIAMETER VS TIME FROM ΔV$_r$
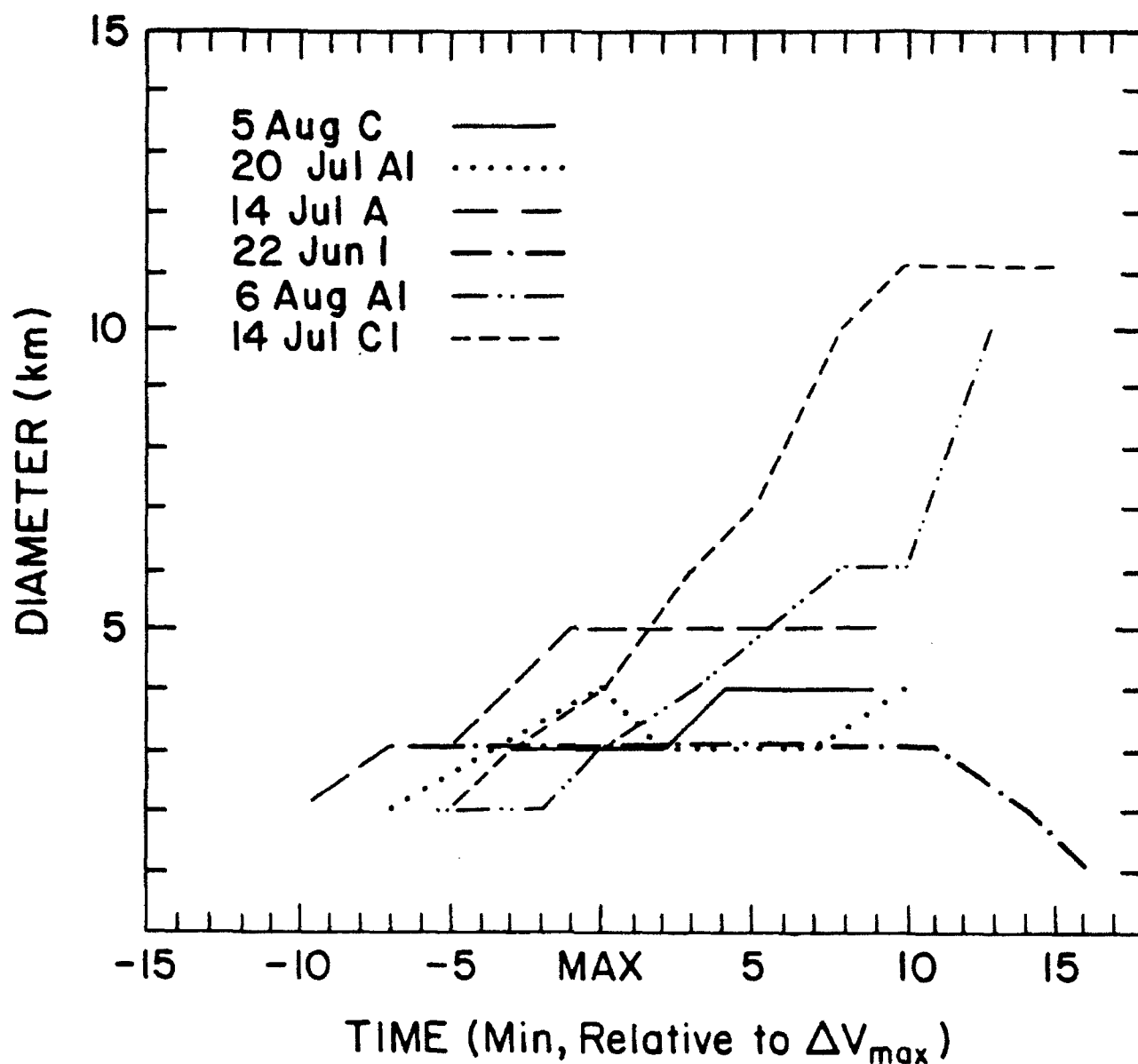
FIGURE 5.2. In this figure, the diameter of the event is plotted against the time from maximum ΔV$_r$ for the identical six cases in Fig. 5.1. Without fail, each microburst grows in diameter somewhat as it approaches maximum strength. After the maximum ΔV$_r$ is reached, the behavior of the six cases diverges dramatically. Some continue to grow into large-scale outflows, while others grow slightly more or remain at the same diameter. One case, 22 Jun 1, starts and remains at the same diameter through its maximum strength, shrinking only at the very end of its life time, while another, 20 Jul A1, shrinks in diameter immediately after reaching maximum strength. The typical behavior of microburst size may only be characterized in the intensification stages, i.e., microbursts tend to grow in size as they reach maximum strength. After reaching maximum strength, typical behavior is not easily described.

VELOCITY AS A FUNCTION OF HEIGHT
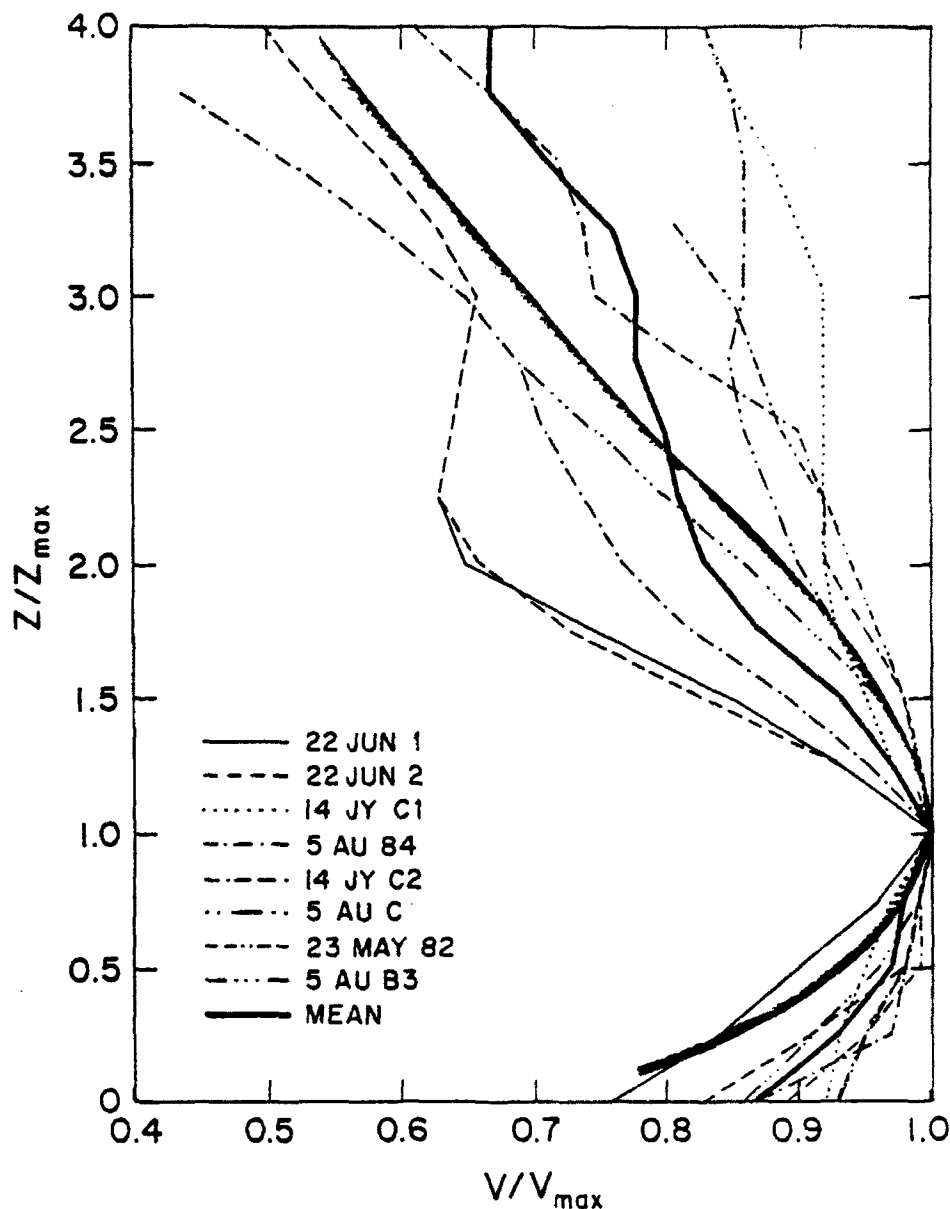
FIGURE 5.3. This figure plots velocity as a function of height through the center of a microburst velocity maximum. All velocities have been normalized to the maximum velocity found in the vertical. Eight microbursts make up the sample; all show very similar structure below the height of maximum velocity. But, as for the decay of ΔV_r after the maximum time and the change in diameter after the time of maximum ΔV_r, these microbursts show markedly different profiles above the height of maximum velocity. The heavy dark line shows the mean for the eight cases plotted, and a velocity profile typical of an impinging wall jet is indicated by the wide grey line. The mean height of maximum outflow winds is 80 m, indicating that if a radar cannot view events very near the ground, there is no way of knowing how strong the event might be. This has serious implications for radar siting. The mean distribution gives some very rough guidance, but in some instances the maximum outflow winds will be under-estimated. However, for ground-based detection systems such as the LLWAS, estimating the maximum outflow speeds above the surface is a relatively straightforward problem.

VELOCITY AS A FUNCTION OF HEIGHT
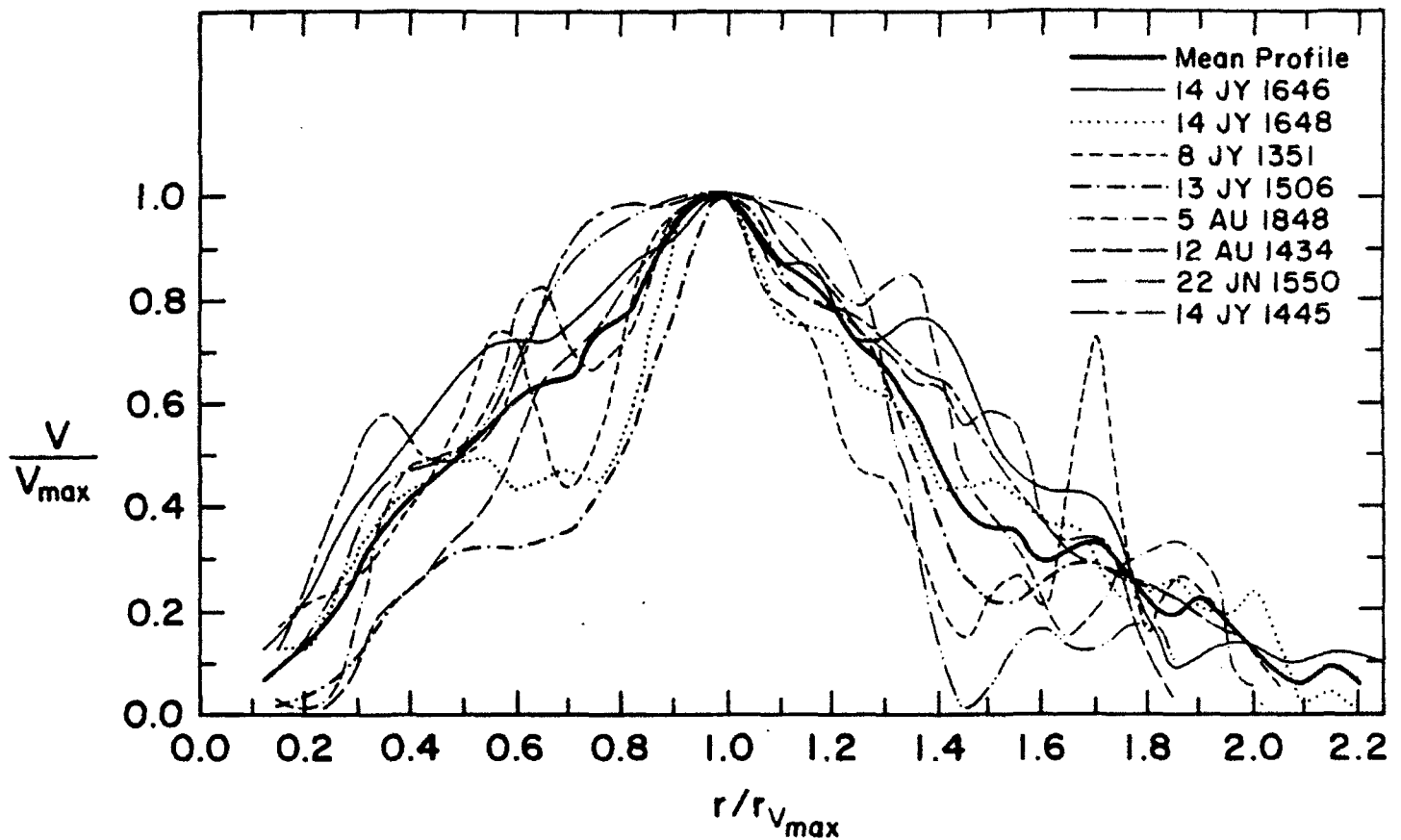
FIGURE 5.4. This figure is similar to Fig. 5.3, except for a horizontal slice through the center of a velocity maximum at a 0° elevation angle. The normalized outflow velocity is plotted against the normalized radius from the center of the microburst. Eight cases are included, and the heavy line shows the mean profile. An interesting characteristic is relative maxima and minima found at large radii. These are believed to be artifacts of horizontal rolls that have been observed visually and through numerical models at the edge of microburst-type outflows. However, each case shows a somewhat different location for the suspected roll vortex signatures. In the mean profile, the roll vortices tend to be smoothed out, and a general region of small slope characterizes their location. Note also that the shape of the distribution resembles a wall jet—an almost linear increase in outflow velocity from the center to the radius of maximum velocity followed by a nonlinear, less steep velocity decay as the radius increases past that of maximum velocity.

SCHEMATIC JAWS MICROBURST STRUCTURE
AT MAXIMUM INTENSITY

FIGURE 5.5. This figure gives an average representation of a microburst at its maximum intensity. The half-tone streamlines are intended as a schematic representation only; any given microburst may not be as symmetric as this. The diameter of the downdraft is about 1.5 km at 1.5 km AGL, and the mean downdraft speed in the center of the downdraft is about 12 m s^{-1}. The average maximum outflow wind strength is 12.7 m s^{-1}, yielding an average ΔV_r of 25.5 m s^{-1}. The average distance from the center of the maximum wind is 1.7 km, and the average height is 80 m AGL. The vertical and horizontal normalized profiles are shown, similar to what has already been presented.

Table 5.1 describes microburst statistics pertaining to detection and warning. Several different categories are used: the average time before first recognized divergence at the ground, the average $\frac{\Delta V_r}{\Delta r}$ at initial detection, the average time before maximum strength of the first alarm, the average $\frac{\Delta V_r}{\Delta r}$ at first alarm, the average maximum $\frac{\Delta V_r}{\Delta r}$, the average time after maximum strength of the last alarm, the average $\frac{\Delta V_r}{\Delta r}$ at the last alarm, and the average outflow depth at maximum intensity. The alarm threshold required for an alarm to be issued must have a ΔV_r of at least 10 m s^{-1}, and the shear must be at least 2.5 $\times 10^{-3}$ s^{-1}.

The average time before maximum strength of the first recognized divergence at the lowest altitude is 6:08, with a standard deviation of 4:00 (all values are given as mm:ss). For this statistic, only eight microbursts out of 26 (31%) were observed before the first-alarm threshold was reached. The temporal sampling interval for these data is 2 min, so to safely detect the existence of a microburst before it reaches the specified first-alarm threshold requires a sampling interval significantly less than 2 min.

The average ΔV_r at first detection is 14.2 m s^{-1} over a distance of 2.0 km, with standard deviations of 7.9 m s^{-1} and 1.1 km. This is a shear significantly above the hazard threshold defined by the alarm criteria.

The average time before maximum strength of the first alarm is 4:10, with a standard deviation of 3:01. There are only 23 microbursts used in this statistic because the other three were at an intensity in excess of the first-alarm threshold.

The average ΔV_r at the first alarm is 18.0 m s^{-1} over 2.3 km, with standard deviations of 6.6 m s^{-1} and 1.1 km. There are only 23 microbursts included in this statistic because the other three were first observed at maximum intensity (at a 2-min update rate).

For the full 26 cases, the maximum $\frac{\Delta V_r}{\Delta r}$ is 23.4 m s^{-1} over 3.4 km, with standard deviations of 6.8 m s^{-1} and 1.4 km. This average is somewhat lower than the average strength of 25.4 m s^{-1} discussed earlier, because not all microbursts used in that average were used in this table.

Twenty-five microbursts decayed to a strength below the alarm threshold in an average interval of 7:27, with a standard deviation of 3:38. The 26th case did not decay below the alarm threshold before scanning was terminated.

Finally, the average $\frac{\Delta V_r}{\Delta r}$ of the above 25 cases at the last alarm is 11.7 m s^{-1} over a distance of 4.3 km (equivalent to a shear of 2.7 $\times 10^{-3}$ s^{-1}), with standard deviations of 5.7 m s^{-1} and 3.0 km.

34

TABLE 5.1 Microburst statistics derived from JAWS radar data.

Parameter	Average, Standard Deviation
Time before max of first recognized divergence at lowest elevation	(26 cases) −6:08, 4:00
$\frac{\Delta V_r}{\Delta r}$ at initial detection	(26 cases) 14.2 m s^{-1}/ 2.0 km, 7.9 m s^{-1}/ 1.1 km
Time before max of first alarm	(23 cases) −4:10, 3:01
$\frac{\Delta V_r}{\Delta r}$ at first alarm	(23 cases) 18.0 m s^{-1}/ 2.3 km, 6.6 m s^{-1}/ 1.1 km
$\frac{\Delta V_r}{\Delta r}$ at max	(26 cases) 23.4 m s^{-1}/ 3.4 km, 6.8 m s^{-1}/ 1.4 km
Time after max of last alarm	(25 cases) 7:27, 3:38
$\frac{\Delta V_r}{\Delta r}$ at last alarm	(25 cases) 11.7 m s^{-1}/ 4.3 km, 5.7 m s^{-1}/ 3.0 km
Outflow depth at max	(21 cases) 0.6 km, 0.2 km

6. Parent Storm Structure

Although not necessarily of direct importance to the pilot, parent storm structure may determine what unique indicators of microburst formation apply. The events that occur in a low-reflectivity storm prior to microburst formation may be substantially different from precursor events associated with medium or high-reflectivity storms. Such information is invaluable when applied to the problem of forecasting microburst formation.

It is important to note that the one feature common to all storm types listed here is convergence, either very near cloudbase or somewhat above cloudbase. However, it should also be noted that such convergence is not a completely reliable indicator of an incipient microburst for high plains storms around Denver; some storms exhibiting such a feature never produce a surface outflow.

The following figures and tables are from Roberts and Wilson (1984, 1987).

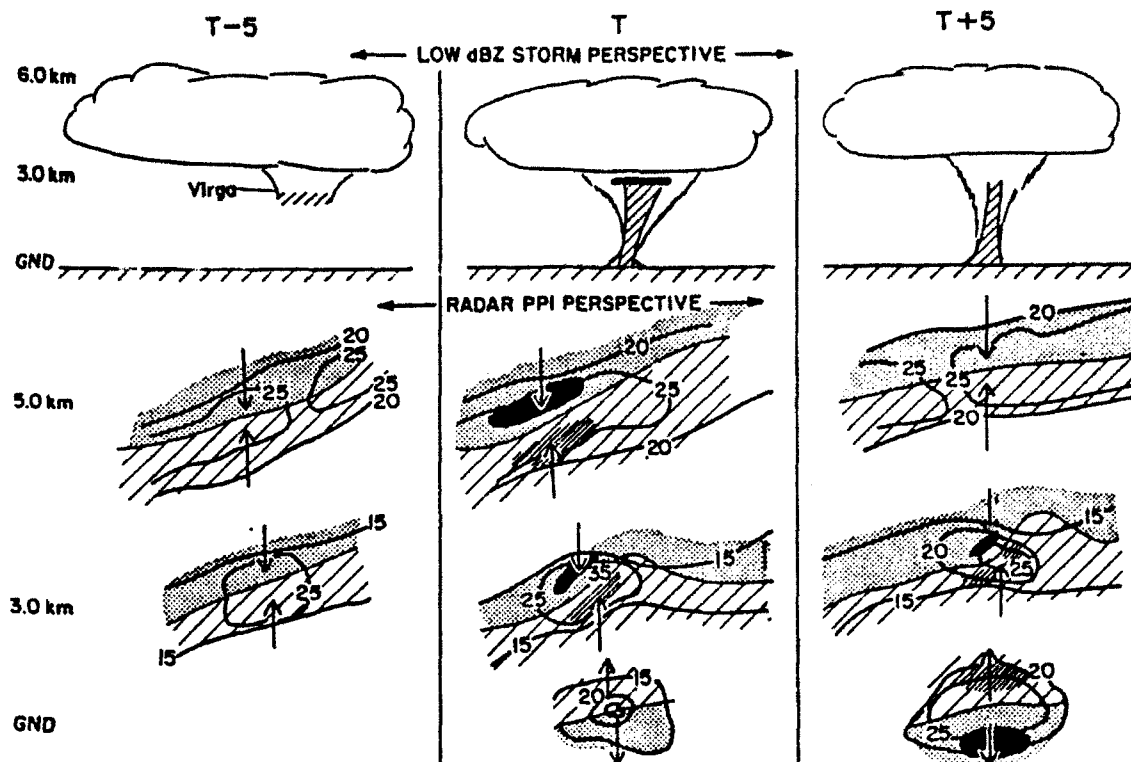# TYPICAL LOW-REFLECTIVITY MICROBURST STORM STRUCTURE

FIGURE 6.1. This figure shows the storm structure typical of low-reflectivity-type microbursts. Low reflectivity is defined here as maximum reflectivity of less than 35 dBZ$_e$ at 500 m AGL within the storm. The upper part of each panel shows the cloud structure at 5 min before the microburst touches down, the time of touchdown, and 5 min after touchdown. The lower part of each panel shows the velocity and reflectivity structure that is typically observed at different heights. The contours denote reflectivity, and the stippled areas indicate velocity away from the radar. The hatched areas indicate velocities towards the radar. Note that for low-reflectivity storms, the cloud tends to be very shallow with little evidence of vertical development.

Five minutes prior to the microburst reaching the ground, virga is typically seen, with little or no precipitation reaching the ground. Maximum reflectivity at 5 km AGL is between 25 and 30 dBZ$_e$; this is also the height of maximum convergence aloft. Some convergence is seen at 3 km AGL.

At the time of maximum intensity, a local maximum in convergence is seen at 5 km AGL. The heavy, short black line beneath the cloud outline in the upper panel is intended to show a radar "bright band" typically observed with these storms. The hatched area shows the downdraft. At 3 km AGL, a "kink" in the reflectivity pattern is often observed, as is rotation. Reflectivity increases at this level to a local maximum of about 35 dBZ$_e$. At the surface, a small area of 20 to 25 dBZ$_e$ may be seen collocated with the center of the outflow.

Five minutes after touchdown, the microburst is near maximum intensity. Some convergence is still evident at 5 and 3 km AGL, and the remnants of the rotation can still be seen in the reflectivity pattern. The outflow is at, or near, maximum at the surface.

37

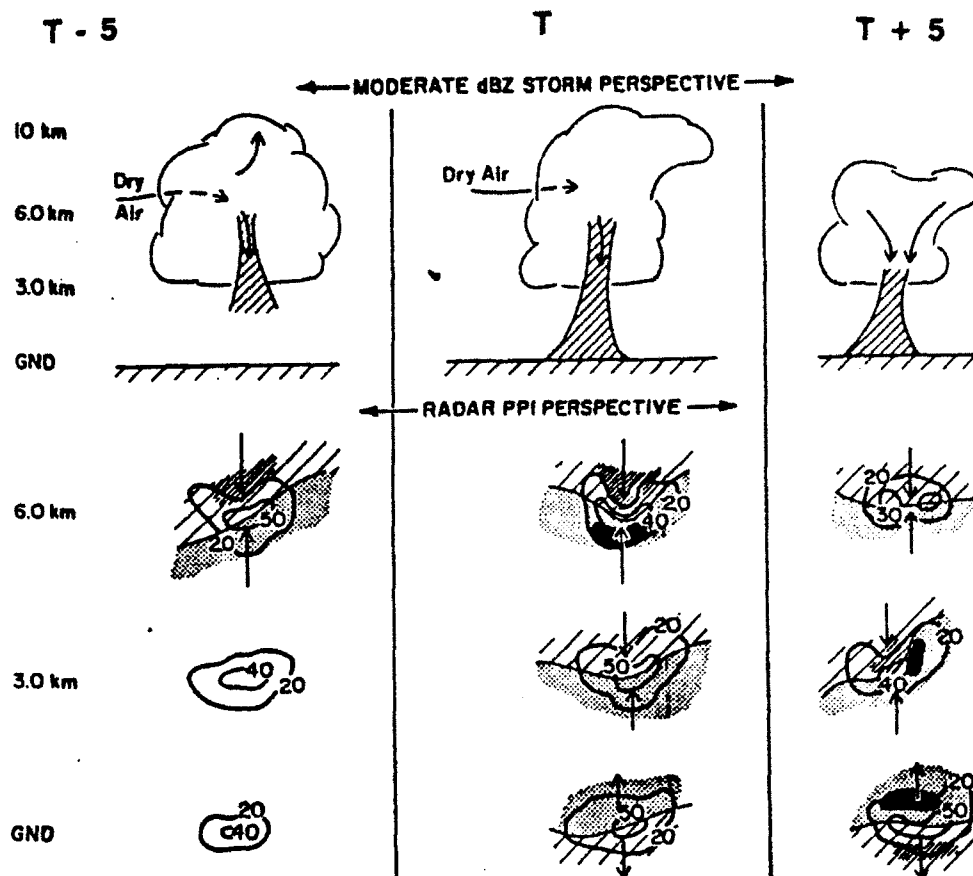# TYPICAL MODERATE REFLECTIVITY MICROBURST STORM STRUCTURE

FIGURE 6.2. Similar to Fig. 6.1, this figure shows structural characteristics typical of moderate reflectivity (between 40 and 55 dBZ$_e$ at 500 m AGL), microburst-producing storms. The top panels show schematic representations of flow within the storm, while the lower panels show typical velocity and reflectivity structures viewed by a single-Doppler radar. The cloud structure for moderate cases shows more vertical development than for the low-reflectivity cases.

Five minutes before touchdown, dry air is entrained into the midlevels of the cloud, around 6 km AGL. This is also the region of maximum observed single-Doppler convergence. A weak echo region, or notch, in the reflectivity is often observed to form in this region. Little or no velocity structure is evident at 3 km or near the ground.

By the time the microburst touches down, a notch in the reflectivity at 6 km is clearly apparent and convergence is at a maximum. A notch also becomes evident at 3 km, as does convergence. Reflectivity at the ground has increased somewhat by this time.

Five minutes after the microburst touches down, the storm begins to collapse. A notch is no longer evident at 6 km, and convergence has weakened substantially. A notch is still observed at 3 km, as is strong rotation. Outflow at the surface is at a maximum.

TYPICAL HIGH-REFLECTIVITY MICROBURST STORM STRUCTURE
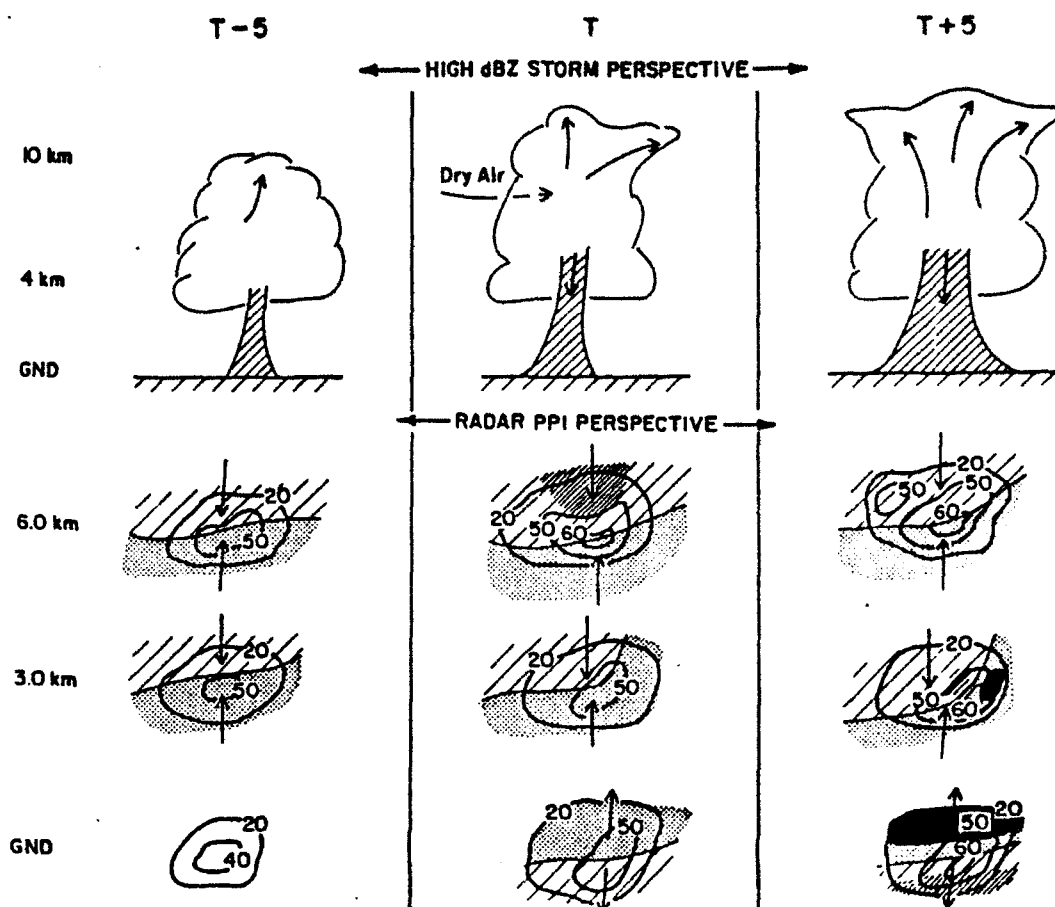
FIGURE 6.3. For high-reflectivity (greater than 55 dBZ$_e$ at 500 m AGL) microburst storms, the cloud shows much stronger vertical development. As for the previous figures, the top panel shows schematic flow and storm structure, while the bottom panel shows a typical single-Doppler perspective.

About 5 min prior to the microburst touchdown, some convergence is seen at 6 and 3 km. No outflow is yet apparent.

When the microburst touches down, environmental air is still being entrained into the storm at midlevels, appearing as convergence at 6 and 3 km. A weak reflectivity notch may be evident near 6 km and may have some rotation at 3 km. Reflectivity at all levels has increased markedly by this time. Note that the updraft is still active within the parent storm.

Five minutes after touchdown, the outflow is nearly at maximum intensity. Reflectivity continues to increase at all levels, especially near the ground. Some rotation is often evident at 3 km. The storm continues to grow, forming a well-developed anvil by this time.

Table 6.1 is a summary of low-reflectivity microburst storm characteristics. Eleven events were investigated that fit this category. Of the eleven, in 91% (10) the reflectivity core was collocated with the center of the microburst. Although some cases showed signs of a descending reflectivity core, there was no conclusive evidence of such.

Only one case showed a structure typical of a collapsing storm, while two cases showed ambiguous or inconclusive signs. Only 36% (4) of the storms exhibited organized convergence above cloudbase. Twenty-seven percent (3) had ambiguous or inconclusive indications. However, all cases exhibited organized convergence near or below cloudbase, as computed from the temporally closest sounding.

Only about one-third of the storms displayed a reflectivity notch, but almost 90% had rotation associated with them. No case exhibited all characteristics.

The additional statistics on low-reflectivity storms that follow are from Kessinger et al. (1986). At least 32 of these types of storms occurred during JAWS. On at least 11 out of 91 operational days of JAWS (12%), low-reflectivity storms occurred. All of these storms occurred between 1300 and 1900 MDT and 75% of these occurred between 1400 and 1700 MDT. The average ΔV_r at maximum intensity was 24 m s^{-1}, with a range of 12 to 50 m s^{-1}. Low-reflectivity microbursts tend to occur in groups; typically three occur per episode, and the low-reflectivity storms actively produce outflows for about 1 hr.

TABLE 6.1. Low dBZ$_e$ storm (below 35 dBZ$_e$ at or below 500 m AGL) statistics.

Parameter	Statistic (number cases)
Number of events	11
Fraction showing reflectivity core co-located with microburst	91% (10)
Fraction displaying descending reflectivity core	no conclusive examples
Fraction showing collapsing structure during outflow	9% (1), while another 18% (2) exhibited inconclusive signs
Fraction showing organized convergence significantly above cloudvase (considered mid-cloud)	36% (4), while another 27% (3) exhibited inconclusive signs
Fraction showing organized convergence near cloudbase (computed from sounding)	100%
Fraction displaying reflectivity notch associated with active cell	36% (4)
Fraction displaying rotation at some height within active cell	82% (9)
Total number of low reflectivity storms catalogued to date	32
Fraction of days with low dBZ$_e$storms of 91 operational JAWS days	12% (11 days)
Time-of-day window in which low-reflectivity microbursts are active	1300-1900
Most common window	1400-1700 (75% of storms, 24 cases)
Average $\triangle V_r$	24 m s^{-1}(12 to 50 m s^{-1})
Average number of microbursts occurring during time of activity	3 (1 to 7)
Episode lifetime	1 hr

TABLE 6.2. Moderate dBZ$_e$ storms (40–50 dBZ$_e$ at or below 500 m AGL) statistics.

Parameter	Statistic (number cases)
Number of events	7
Fraction showing reflectivity core co-located with microburst	100% (13)
Fraction showing descending reflectivity core	57% (4)
Fraction showing collapsing structure during outflow	100% (7)
Fraction showing organized convergence significantly above cloudbase (considered mid-cloud)	100% (7)
Fraction showing organized convergence near cloudbase (computed from sounding)	100% (7)
Fraction displaying reflectivity notch associated with active cell	43% (3)
Fraction displaying rotation at some height within active cell	71% (5)

Table 6.2 is similar to Table 6.1 for moderate reflectivity storms. Seven storms fit into this category. All storms displayed a reflectivity core collocated with the microburst, all storms possessed a collapsing structure while the outflow was active, and all displayed organized convergence above cloudbase, near midlevels.

Only about one-half (57%) displayed a descending reflectivity core. Fewer yet (43%, 3 storms) displayed organized convergence near or below cloudbase. The same proportion exhibited a reflectivity notch, while 71% possessed rotation at some point around the time the outflow was active. For this set of storms, only two possessed all of the above characteristics. These two cases occurred on different days separated by about one month.

TABLE 6.3. High dBZ$_e$ storm (greater than 55 dBZ$_e$ at or below 500 m AGL) statistics.

Parameter	Statistic (number cases)
Number of events	13
Fraction showing reflectivity core co-located with microburst	100% (13)
Fraction showing descending reflectivity core	37% (4)
Fraction showing collapsing structure during outflow	0% (0)
Fraction showing organized convergence significantly above cloudbase (considered mid-cloud)	23% (3), while an additional 15% (2) showed inconclusive signs
Fraction showing organized convergence near cloudbase (computed from sounding)	69% (9)
Fraction displaying reflectivity notch associated with active cell	46% (6)
Fraction displaying rotation at some height within active cell	62% (8)

Thirteen high-reflectivity-type microburst storms were thoroughly investigated. All showed the reflectivity core collocated with the microburst. Only 31% (4 storms) clearly displayed a descending reflectivity core, and none possessed characteristics typical of a collapsing storm while the outflow was active. Only three storms (23%) had organized convergence above cloudbase (near midlevels), while two storms displayed ambiguous signs. Most (9 storms, 69%) had organized convergence near or below cloudbase. About one-half (46%) displayed a reflectivity notch and a little more than one-half (62%, 8 storms) had rotation aloft. Of all of these cases, only one displayed all characteristics except for the collapsing structure.

7. Microburst Lines

Microburst lines consist of several microbursts line-abreast, much as a squall line consists of several thunderstorms line-abreast. Just as in a squall line, the individual lifetime of each element is typically less than the lifetime of the entire entity.

Microburst lines are treated as a special subset of the total microburst problem for several reasons. Microburst lines tend to be quite long-lived when compared to their isolated counterparts. On the average, they also tend to be somewhat stronger than isolated events, and microburst lines can affect much larger areas than do single microbursts. Thus, a microburst line has a much greater potential for affecting air traffic operations around an airport than does a single, isolated microburst.

The following data and statistics are from Hjelmfelt (1987). The reader should keep in mind that many more statistics than presented here have been examined. Means and standard deviations are presented in Table 7.1, but correlations between any two parameters in the table not specifically mentioned in the following figures either have not been investigated or are insignificant.

TABLE 7.1. Microburst line statistics for 19 individual microburst lines.

Parameter	Average, Standard Deviation or Range
Lifetime	48.7 min, 28.8 min
Time to max	18.6 min, 14.1 min
Max ΔV	27.3 m s^{-1}, 9.6 m s^{-1}
Width across peak-to-peak ΔV	3.26 km, 0.8 km
End-to-end length	17.3 km, 7.4 km
Outflow depth	1.7 km, 0.9 km
Number of microbursts contained within line over entire lifetime	2.9, range of 2-4
Number of microbursts contained within line at max time	3.7, range of 2-6
Reflectivity within strongest core at 500 m AGL	48.7 dBZ$_e$ 16.5 dBZ$_e$
Line translation speed	1.2 m s^{-1}, 2 m s^{-1}
Microburst spacing	6.0 km, 2.7 km
Individual microburst lifetime	15 min

This table gives basic statistics for microburst lines. By definition, a microburst line must be made up of at least two microbursts. The average lifetime of a microburst line is 48.7 min, with a standard deviation of 28.8 min. The average period from first divergence at the surface to the maximum observed divergence is 18.6 min, with a standard deviation of 14.1 min. The average maximum ΔV_r across the line is 27.3 m s^{-1}, with a standard deviation of 9.6 m s^{-1}. This is slightly stronger than that for individual microbursts (23.4 m s^{-1}), as shown in Table 5.1. The average distance across the velocity maxima when the line is strongest is almost the same as for individual microbursts: 3.3 km, with a standard deviation of 0.8 km for lines compared to 3.4 km, with a standard deviation of 1.4 km for isolated microbursts. The typical length of a line is 17.3 km, with a standard deviation of 7.4 km. Outflow depth for lines averages to 1.7 km, with a 0.9 km standard deviation. Throughout their lifetime, lines contain 2.9 microbursts on the average (displaying a range of 2 to 4). At maximum intensity, lines contain an average of 3.7 microbursts, ranging anywhere from 2 to 6. At 500 m AGL, the average reflectivity at maximum outflow intensity is 48.7 dBZ$_e$, with a standard deviation of 16.5 dBZ$_e$. Microburst lines do not display much motion, with an average translation speed of 1.2 m s^{-1} and a standard deviation of 2.0 m s^{-1}. Finally, the average spacing of microbursts along the line at maximum outflow intensity is 6.0 km, with a standard deviation of 2.7 km. Microburst lines tend to last considerably longer than single, discrete microbursts. Also, lines that contain a large number of microbursts (5 or more) are likely to be strong.
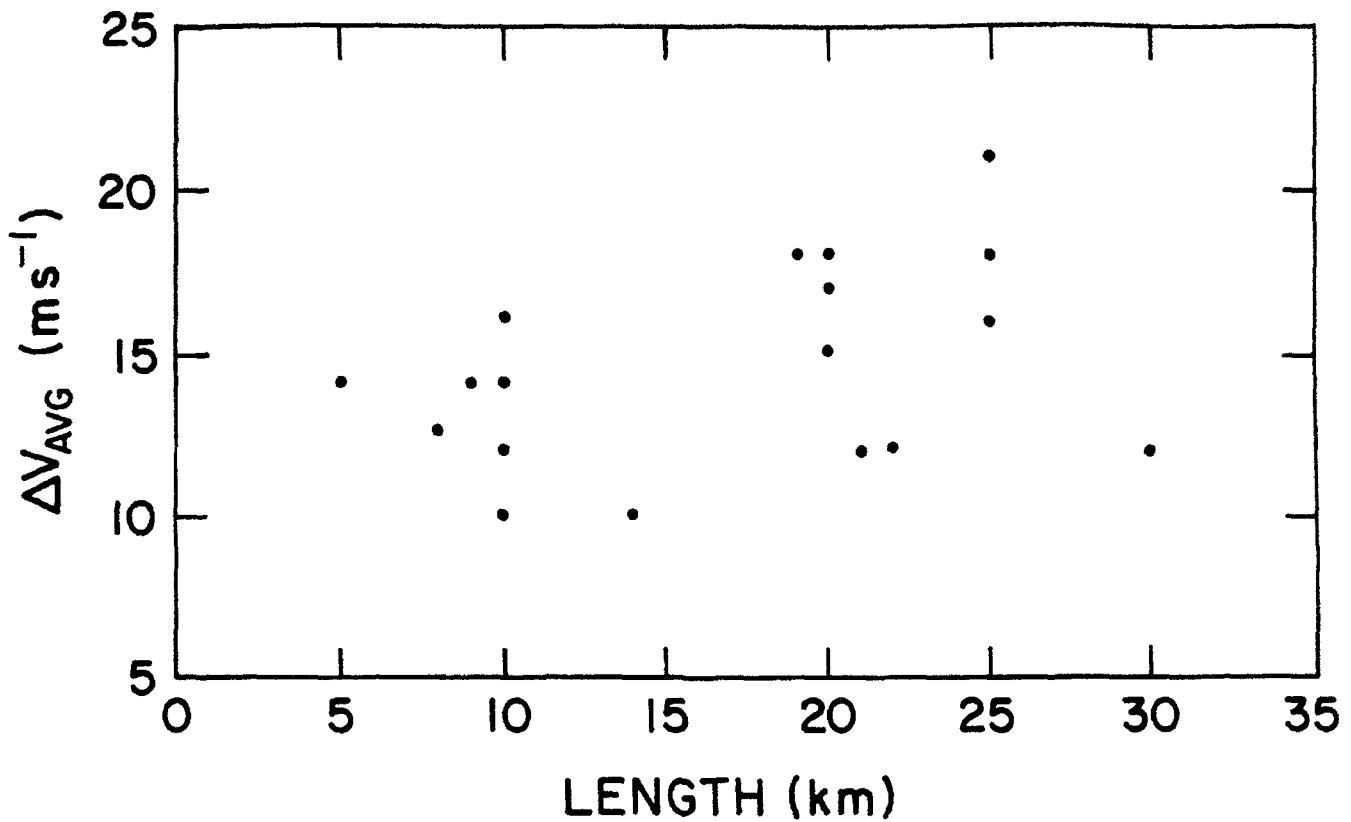
45

ALONG-LINE AVERAGE ΔV
vs. LINE LENGTH

FIGURE 7.1. This figure shows the average ΔV_r averaged along the microburst line as a function of the line length. In this case, there is a weak correlation, suggesting that the longer lines may contain stronger divergence. However, there is considerable scatter, indicating that line length is not a reliable method of determining the degree of hazard.

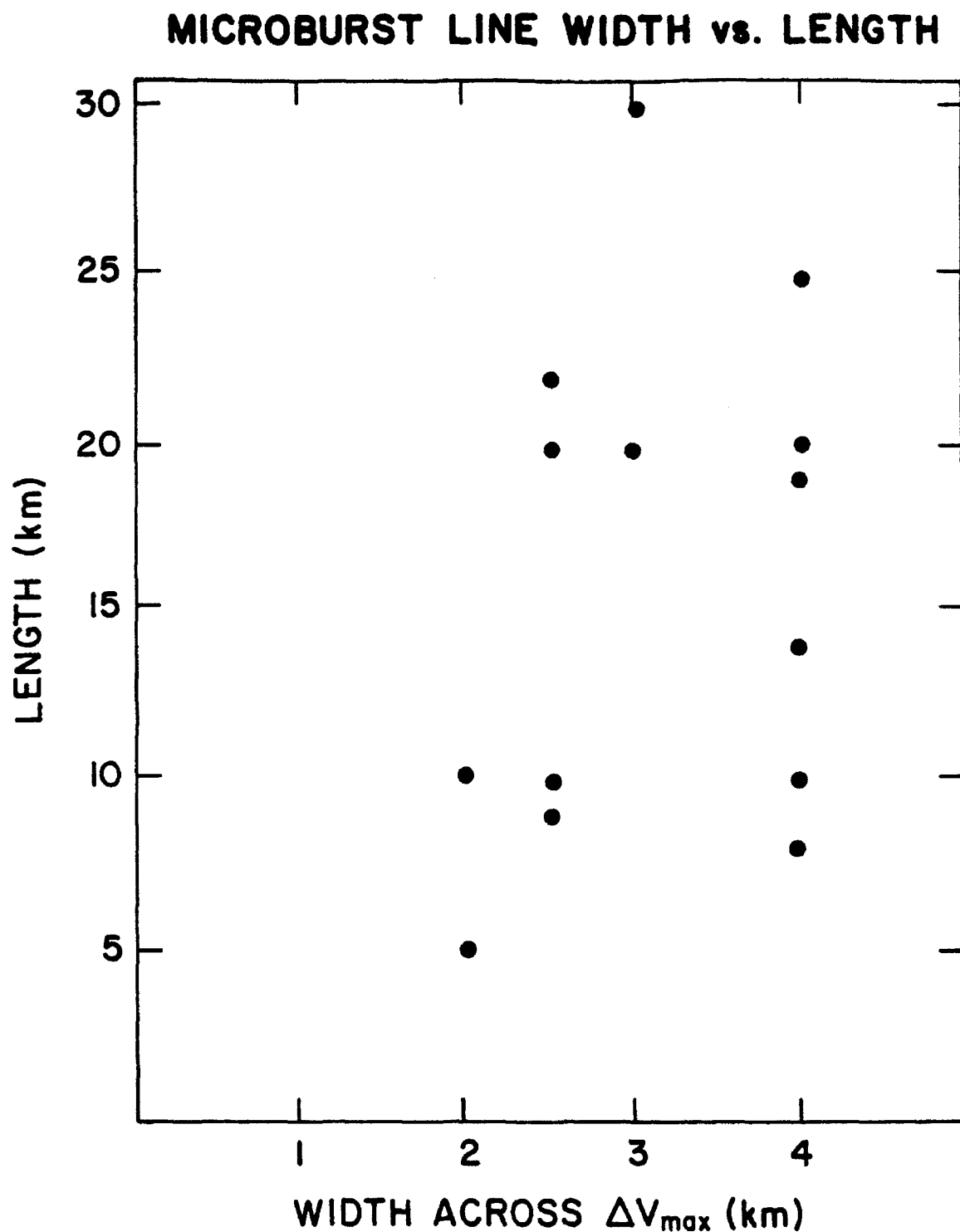# MICROBURST LINE WIDTH vs. LENGTH

FIGURE 7.2. This figure shows line length plotted as a function of line width. Line width is defined as the average distance between velocity maxima along the line. There is no correlation between the two parameters; a line of a particular width can be almost any length. There is no characteristic aspect ratio.
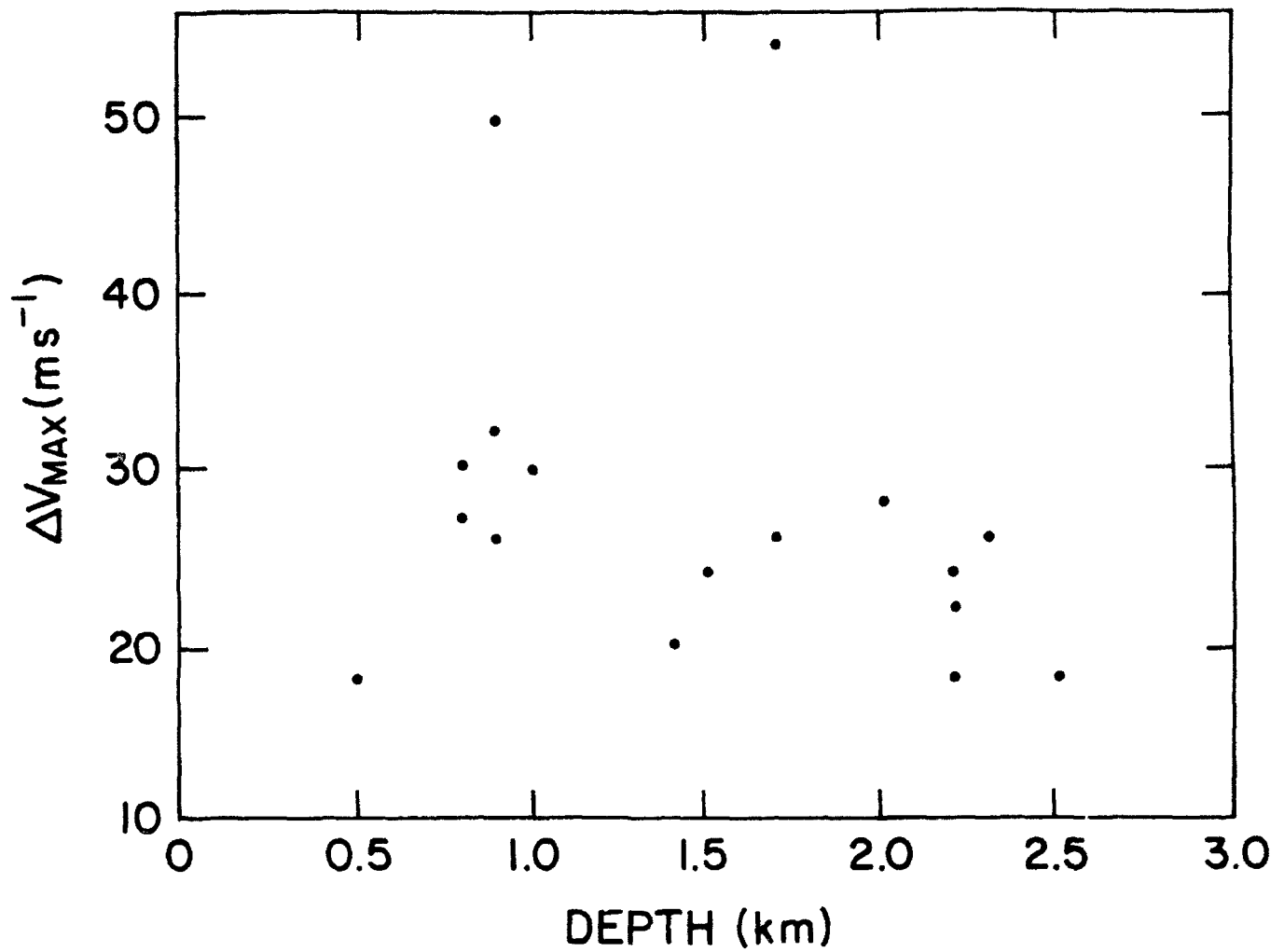
OUTFLOW DEPTH vs. MAXIMUM ΔV

FIGURE 7.3. In this figure, the maximum ΔV_r is plotted as a function of the outflow depth. As before, the two show no clear correlation. The depth of the outflow cannot be determined from the strength of the outflow.
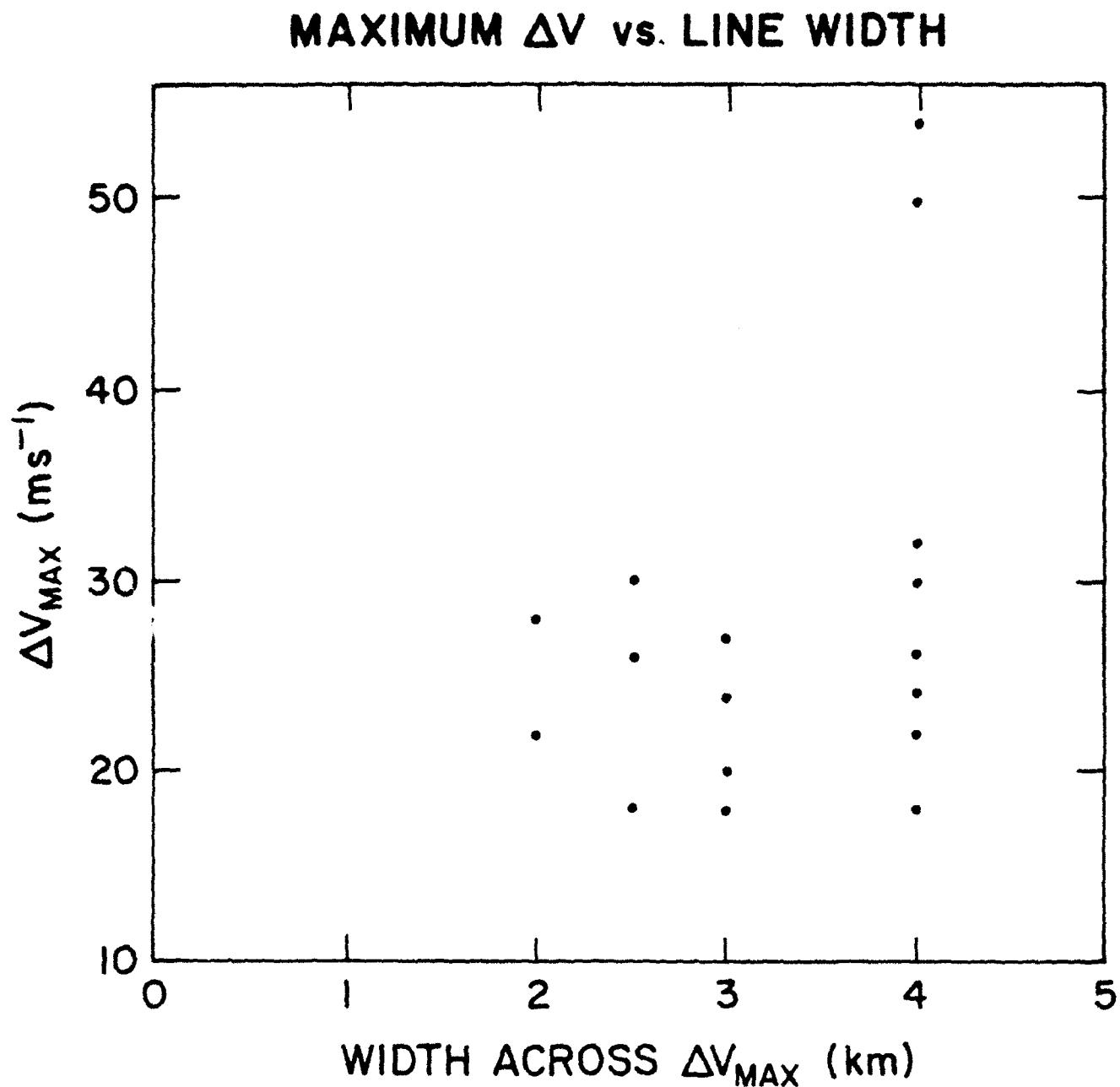
MAXIMUM ΔV vs. LINE WIDTH

FIGURE 7.4. Maximum ΔV_r across the lines is plotted as a function of line widths. Again, there is no correlation; the width of a line is not a good indicator of the maximum ΔV_r that it may contain. There are comparatively few cases in this statistic. It is suspected that if sufficient data were available and a plot similar to Fig. 3.5 were made, some correlation would be exhibited. However, the added complexity of each point representing some combination of two or more microbursts would almost certainly increase the scatter, possibly reducing any correlation below significant levels.

ACKNOWLEDGMENT

REFERENCES

Bedard, A. J., and T. J. LeFebvre, 1986: Surface measurements of gust fronts and microbursts during the JAWS project: Statistical results and implications for wind shear detection, prediction and modeling. NOAA Tech. Memo. ERL WPL-135, NOAA, Boulder, Colo., 112 pp.

Hjelmfelt, M. R., 1987: Structure and life cycle of microburst outflows observed in Colorado. *J. Clim. Appl. Meteor.*, **27**, 900–927.

Kessinger, C. J., R. D. Roberts and K. L. Elmore, 1986: A summary of microburst characteristics from low-reflectivity storms. *Preprints, 23rd Conf. on Radar Meteor.*, Snowmass, Colo. Amer. Meteor. Soc., Boston, Mass., J105–J108.

Roberts, R. D., and J. W. Wilson, 1987: Nowcasting microbursts using Doppler radar in a forecaster-computer environment. *Proc. Symp. Mesoscale Analysis & Forecasting*, Vancouver, Canada. Amer. Meteor. Soc., Boston, Mass., 43–48.

Roberts, R. D., and J. W. Wilson, 1984: Precipitation and kinematic structure of microburst producing storms. *Preprints, 22nd Radar Meteor. Conf.*, Zurich, Switzerland. Amer. Meteor. Soc., Boston, Mass., 71–76.

Wilson, J. W., R. D. Roberts, C. J. Kessinger and J. McCarthy, 1984: Microburst wind structure and evaluation of Doppler radar for airport wind shear detection. *J. Clim. Appl. Meteor.*, **23**, 898–915.